EUROPEAN ORGANIZATION FOR NUCLEAR RESEARCH

CERN-EP/81-04
20 January 1981

DIFFRACTIVE PRODUCTION OF STRANGE MESONS AT 63 GeV

C. Daum, L. Hertzberger, W. Hoogland, S. Peters and P. Van Deurzen,

NIKHEF-H, Amsterdam, The Netherlands

V. Chabaud, A. Gonzalez-Arroyo, B. Hyams, H. Tiecke[1] and P. Weilhammer,

CERN, Geneva, Switzerland

A. Dwurazny, G. Polok, M. Rozanska, K. Rybicki, M. Turala and J. Turnau,

Institute of Nuclear Physics, Cracow, Poland

H. Becker, G. Blanar, M.Cerrada[2], H. Dietl, J. Gallivan, R. Klanner,

E. Lorenz, G. Lütjens, G. Lutz, W. Männer and U. Stierlin,

Max-Planck Institut für Physik und Astrophysik, Munich, Fed. Rep. Germany

I. Blakey, M. Bowler, R. Cashmore, J. Loken, W. Spalding[3] and G. Thompson[4],

University of Oxford, England

B. Alper[5], C. Damerell, A. Gillman, C. Hardwick, M. Hotchkiss and F. Wickens,

Rutherford Laboratory, Chilton, England

(The ACCMOR Collaboration)

(Submitted to Nuclear Physics B)

1 Now at NIKHEF-H, Amsterdam, The Netherlands.
2 Now at CERN, Geneva, Switzerland.
3 Now at Toronto University, Canada.
4 Now at Queen Mary College, University of London, England.
5 Now at ETSU, Harwell, England.

ABSTRACT

Nearly 200,000 examples of the diffractive process $K^-p \to K^-\pi^-\pi^+p$ at 63 GeV have been obtained using a two-magnet spectrometer equipped with Čerenkov counters for secondary particle identification. In addition, some 2,000 examples of the process $K^-p \to \omega K^-p$ have been obtained. The $K\pi\pi$ data have been subjected to partial-wave analysis. The dominant $J^P = 1^+$ system couples to $K^*\pi$ (in both the S-wave and the D-wave), ρK, $\kappa\pi$, and εK. The data confirm the existence of two $J^P = 1^+$ Q mesons, and their masses, widths, and branching ratios are given. The ωK data show that the couplings of the Q mesons to ωK are approximately equal to the couplings to $\rho^0 K$. The two 1^+ nonets expected in the quark model are discussed in the light of this and other recent experiments. There is strong evidence for a broad $J^P = 0^-$ resonance at about 1.46 GeV. At higher masses, the structure in the $J^P = 2^-$ partial waves establishes the existence of at least one $J^P = 2^-$ L meson.

1. INTRODUCTION

The first high-statistics study of the diffractive processes

$$K^{\pm}p \to K^{\pm}\pi^-\pi^+p$$

was carried out at SLAC, using a 13 GeV incident $K^{\pm}$ beam and a magnetic spectrometer with Čerenkov identification of the secondaries [1]. The data were sufficient for partial-wave analysis up to a $K\pi\pi$ mass of 1.6 GeV. The results were interpreted in terms of diffractive production of two $J^P = 1^+$ Q mesons, with masses of 1.27 and 1.41 GeV, together with a diffractively produced background. These inferences were supported by two independent analyses [2,3] of the $J^P = 1^+$ results in terms of models in which two 1^+ mesons are diffractively produced, both directly and through rescattering of a Deck background [4]. The SLAC group also observed the $K^*\pi$ decay mode of the 2^+ $K^*(1430)$ and found evidence suggestive of a broad 0^- resonance at a mass $\sim$ 1.4 GeV.

In early 1977, a multiparticle spectrometer [5] was set up by this collaboration in the West Area at CERN (SPS experiment WA3). This spectrometer contained two Čerenkov counters for secondary particle identification and was fed with an unseparated beam of up to 100 GeV, having differential Čerenkov counters for particle identification. The beam contained approximately 4% K^- at 63 GeV, and in the course of a long run during which the main trigger was for the reaction

$$\pi^-p \to \pi^-\pi^+n$$

almost 200,000 examples of the reaction

$$K^-p \to K^-\pi^-\pi^+p \text{ at 63 GeV}$$

were accumulated parasitically. These data are sufficient for partial-wave analysis extending up to a mass of 2.1 GeV, and complement the data on diffractive production of three-pion states also obtained with this spectrometer [5-8].

During part of the run, a photon calorimeter at the downstream end of the spectrometer detected additional π^0's, and 2025 events from the reaction $K^-p \to K^-\omega p$ with $(\omega \to \pi^+\pi^-\pi^0)$ were acquired.

The $J^P = 1^+$ system, dominant at low mass, has been observed in six different final states: $K^*\pi$ (S- and D-wave), ρK, $\kappa\pi$, εK, and ωK. The existence of two 1^+ Q mesons is confirmed, and their masses, widths, and branching ratios are given. The data contain strong evidence for a 0^- meson with a mass $\sim$ 1.46 GeV, and, in addition to the $K^*\pi$ decay of the 2^+ $K^*(1430)$, the ρK mode has also been detected. This experiment has confirmed the essential features of the SLAC data, and new results have been obtained in the range $1.6 < M_{K\pi\pi} < 2.1$ GeV. The $J^P = 2^-$ system couples to $K^*(1430)\pi$, fK, and to P-wave $K^*\pi$: the structure in these amplitudes reveals the presence of at least one diffractively produced 2^- L meson.

The spectrometer and significant aspects of data reduction are discussed in Section 2. Section 3 deals primarily with the 1^+ system in the Q region, including an analysis in terms of what has become the standard model of the Q complex, while the high-mass region is discussed in Section 4. The structure of the two 1^+ nonets expected on the basis of the quark model is discussed in Section 5, in the light of this and other recent experiments.

2. APPARATUS, DATA TAKING, AND DATA REDUCTION

2.1 The spectrometer

The spectrometer [5] is shown in fig. 1. The 50 cm liquid-hydrogen target was surrounded with a box of lead/scintillator sandwich counters (F) and followed by the first pack of magnetostrictive wire spark chambers (S1). The first magnet M1 had an effective aperture of 2 m × 0.4 m and a bending power of 8.5 kG•m. It was followed by the double scintillator hodoscope P2/3, and separated from the second magnet M2 by the second pack of spark chambers S2. The second magnet had an aperture 1.5 × 0.5 m and a bending power of 20 kG•m. This two-magnet configuration ensured high acceptance and good momentum resolution for both low- and high-energy secondaries. After the second magnet came the last three packs of spark chambers (S3-5), separated by two multicell threshold Čerenkov counters.

The components of the spectrometer have already been discussed in detail in ref. 5, except for the photon calorimeter described in the next section.

2.2 The photon calorimeter

In order to measure reactions with neutral pions in the final state, a photon calorimeter [9] was installed for the second half of the data-taking period. The calorimeter was placed just after the last pack of spark chambers, about 25 m from the target (see fig. 1).

The calorimeter consisted of two identical blocks of 40 scintillator planes with 2 cm wide elements, interleaved with layers of lead, 4 mm thick. The construction is shown in fig. 2. The two blocks together covered an area 3×1.5 m^2 perpendicular to the beam. Planes with horizontal and vertical strips were alternated, and all 20 strips at a given horizontal or vertical position were brought to a common light-guide to form a fork with 20 prongs. The outputs from the photomultipliers looking at each fork were fed into 12-bit ADCs and read into the on-line NORD-10 computer.

The calorimeter was approximately 28 radiation lengths deep, and each fork sampled all depths. On the average, 95% of the total energy in an electromagnetic shower was deposited within three adjacent forks in each plane. The calorimeter was calibrated with electron beams at 15, 30, and 60 GeV, the shower energy and position being compared with the values obtained from the spectrometer spark chambers for individual electrons. The energy of a single shower could be obtained independently from either the horizontal or the vertical forks, and the resolution on the average of the two measurements of energy is well represented by

$$\sigma(E)/E = 0.015 + 0.14/\sqrt{E} \qquad (E \text{ in GeV}) \ .$$

The spatial resolution in determining the shower axis was $\sim$ 2.5 mm.

2.3 Data-taking

The arrival of a beam particle was signalled by a coincidence (UB) between three small counters in the beam, in anticoincidence with two counters with holes for the beam to pass through. Kaons were identified by requiring at least six out of eight cells to fire in a CEDAR differential Čerenkov counter set for kaons. The trigger for both $K^-p \to K^-\pi^-\pi^+p$ and $K^-p \to K^-\pi^-\pi^+\pi^0p$ required three hits in the

double scintillator hodoscope P2/3, more than one hit in at least one of the two planes of proportional wire chambers P1, and no hits in any of the lead/scintillator sandwich counters (G), which intercepted wide-angle secondaries. The last condition reduced the trigger rate by a factor of 2 but reduced the real events by only 11%. The trigger condition was thus

$$\text{MASTER} = \text{UB}\cdot(\text{CEDAR} = \text{K})\cdot(\text{P1} > 1)\cdot(\text{P2/3} = 3)\cdot\bar{\text{G}} \ .$$

On receipt of a MASTER signal the spark chambers were fired and the contents of all counter bit pattern units and ADCs, the proportional wire chamber information, and the spark chamber information were read into the NORD-10 computer and subsequently written on to tape.

The information from the F counters surrounding the target was used off line in the mode ST2 of ref. 5 to reduce the small proportion of $K\pi\pi$ events with an N^* recoiling against the fast secondaries, and the multicell Čerenkov counter information was used off line for secondary particle identification.

Events from a total of 1.6 million triggers were written on to NORD tapes and analysed with the track-finding program TENPRO [5]. Those events with three charged secondaries, one vertex within the hydrogen target, charge balance, and, for $K\pi\pi$ events, a missing mass squared recoiling against the three charged secondaries between -3 and +5 GeV^2, were written onto a condensed data summary tape. These events comprised approximately 20% of all triggers.

2.4 Čerenkov identification

The multicell Čerenkov counters C1 and C2 had nominal thresholds for pions of 8 GeV and 17 GeV, respectively. The response of the Čerenkov counters to secondaries from events with primary kaons is shown in fig. 3 as a function of secondary particle momentum. Identification of each secondary was carried out off-line, combining the information from both Čerenkov counters. Inefficiencies due primarily to threshold effects, to two secondaries pointing at the same Čerenkov mirror, or to a secondary not traversing the full length of a counter, were taken into account during partial-wave analysis, as discussed in ref. 5. The rules adopted for identification of single tracks are given in table 1.

In 76% of the events, sufficient information was available, on combining Čerenkov data for all three tracks, to identify the event. The rules are given in table 2. Those categories given in the first column are uniquely $K^-\pi^-\pi^+$ with the kaon known. The second column contains impossible categories which resulted from misidentification of secondaries with momenta close to a Čerenkov threshold. The third column contains genuine ambiguities constituting 13% of the events accepted as $K\pi\pi$. Since less than 3% of all events were $K^-K^-K^+$ or $K^-p\bar{p}$, these ambiguous events were all accepted as $K\pi\pi$.

The remaining 24% of events were rejected and this was accounted for by rejecting their analogues generated by Monte Carlo methods at a later stage of the analysis.

2.5 Extraction of $K^-\omega p$ events

Events from the reaction

$$K^-p \to K^-\omega p \; ; \quad \omega \to \pi^+\pi^-\pi^0$$

gave the same trigger as $K\pi\pi$ events. The missing mass recoiling against the three fast charged particles was large because of the presence of a fast π^0, and such events could be completely reconstructed if the two photons from π^0 decay were detected in the photon calorimeter. The calorimeter data were analysed with the aim of extracting, with high efficiency, those events with a single π^0.

First, the contents of the photomultiplier ADCs for each fork were translated into energies and sorted into clusters of adjacent horizontal and vertical elements with output exceeding a chosen threshold. The cluster energy was taken as the sum over the central three elements of the cluster. A minimum energy of 3 GeV was required in any cluster.

Showers due to hadron interactions in the calorimeter could be removed if the shower coordinates matched those of a charged particle, extrapolated to the calorimeter. Such a pair of clusters was rejected only if the energies in the horizontal and vertical clusters matched within 5 GeV: if this criterion was not satisfied, the pair was kept because of the possibility of a photon overlapping with a hadron

shower in one projection. The residual loss from this source has been estimated to be $\lesssim$ 5%, using Monte Carlo methods.

In order to obtain the position of a photon and the best estimate of its energy, the horizontal and vertical clusters were paired. The main criterion was a match between energies E_H and E_V obtained from the clusters of horizontal and vertical elements. A good match was defined using the quantity

$$K^2 = \left(\frac{E_H - E_V}{E_H + E_V}\right)^2 ,$$

and the cut adopted was $K^2 < 0.04$. This was determined by taking all possible photon pairs and calculating the effective masses. The resulting mass spectrum contained a clean π^0 signal, and the cut on K^2 was adjusted to optimize acceptance and the signal-to-background ratio. The loss of photons due to the K^2 cuts was estimated to be < 5%.

For every event all possible combinations of horizontal and vertical clusters were considered, and the set containing the minimum number of unpaired clusters was selected. When several combinations gave the same number of unpaired clusters, the one with the smallest value of ΣK^2 was adopted.

The $\gamma\gamma$ effective mass for all events with at least two reconstructed γ's is shown in fig. 4a. There is a prominent π^0 signal over a smooth background, and the π^0 mass resolution is $\sigma \sim 10$ MeV. Figure 4b shows the $\pi^+\pi^-\pi^0$ mass spectrum. The simple requirement of longitudinal momentum balance (fig. 4c) yielded the clean ω signal shown in fig. 4d.

2.6 Final data sample

The final $K\pi\pi$ data sample consisted of 190,567 $K\pi\pi$ events from 1,597,849 triggers. Some events of the type $K^- \to \pi^-\pi^+\pi^-$ and $K^0_S \to \pi^+\pi^-$ (from the reaction $K^-p \to \bar{K}^0\pi^-p$) were accepted in the trigger and used for calibration purposes. Figure 5 shows the 3π mass spectrum for the K^- decay and the $\pi^+\pi^-$ mass spectrum for the K^0_S decay, together with the distribution of missing mass squared recoiling against the three fast secondaries for the $K\pi\pi$ events. The single track momentum

resolution of the spectrometer was $\sim 0.5\%$, resulting in a $K\pi\pi$ mass resolution $\sigma \sim 10$ MeV in the Q region.

The F veto counters reduced the N^* contamination to $\lesssim 5\%$, removing only 5% of the good events. Figure 6 shows the $K^-\pi^+$ and $\pi^-\pi^+$ mass spectra. The $K^*(890)$ is dominant, but there are clear $K^*(1430)$ and ρ^0 signals, and the $\pi^-\pi^+$ mass spectrum displays a shoulder due to the f meson.

The acceptance of the apparatus is shown in fig. 7 as a function of both $K\pi\pi$ mass and four-momentum transfer squared to the recoiling proton, t' ($t' = t - t_{min}$). The trigger acceptance is approximately 60% except at low $K\pi\pi$ mass, where the increased losses are due to the increasing likelihood of two secondaries going through the same element of the P2/3 hodoscope. This figure includes both the geometrical effects (loss $\sim 1\%$ from the aperture of the apparatus and $\sim 16\%$ from P2/3) and the losses from interactions and decay of the charged secondaries ($\sim 15\%$). The additional F counter and Čerenkov identification conditions reduce the final acceptance to $\sim 40\%$.

The $K\pi\pi$ mass spectrum is shown in fig. 8. The $K\pi\pi$ spectrum has a clear double peak on the massive Q-region enhancement, and a further peak in the L region (~ 1.8 GeV). The lower mass part of the Q region is produced with a steeper t dependence than the upper part, and the distribution in t has a break in slope at $|t| \sim 0.4$ GeV^2 (fig. 9), effects which are also present in the analogous case of 3π diffractive production [5]. The variation of the t slope with $K\pi\pi$ mass is shown in fig. 10.

The final $K\omega$ sample consisted of 2025 events from approximately 800,000 triggers. The trigger and Čerenkov identification losses were essentially identical to those for the $K\pi\pi$ sample, but the F counters were not used to remove N^* contamination, a cut on the missing mass recoiling against the $K\omega$ system between -2 and 3.8 GeV^2 being imposed. Losses of π^0's due to one or both photons missing the calorimeter, together with the requirement that the measured energy of any one photon exceed 3 GeV, amounted to a factor of 3.5, and conversion of photons before

reaching the calorimeter contributed a further loss factor of 1.3. The final acceptance for $K\omega$ events was thus approximately 9%. The loss of π^0's in the photon pairing process is not accurately known, but does not exceed 10%.

The raw $K\omega$ mass spectrum is shown as an insert in fig. 8. The Q enhancement is clearly visible, rising very sharply from $K\omega$ threshold, an effect which has also been seen in the data of ref. 10.

2.7 Partial-wave analysis

The $K\pi\pi$ data were analysed in terms of three-particle partial waves, using a program derived from LBL-SLAC [11] in which the fitting variables are partial-wave amplitudes rather than density matrix elements as in the Illinois approach [12]. Two sets of amplitudes (labelled flip and non-flip in table 3) were included, and summed incoherently. Since polarization information on the initial and final protons is not available, the assumption that at least one partial-wave amplitude is purely non-flip must be made. The dominant set is labelled non-flip because the spin of the target proton is not expected to flip in diffractive processes and because the data show no sign of the distribution in t' turning over at small values of $|t'|$. The presence of amplitudes labelled flip will absorb possible sources of incoherence other than proton spin-flip [13].

The use of amplitudes as fitting variables has the advantage of being more highly constrained than fitting in terms of the much greater number of density matrix elements. This is particularly important for dealing with the $K\pi\pi$ system, where the number of independent partial waves is greater than in the analogous 3π system. These extra constraints allow the measurement of the relative phase of different waves containing the same isobar (for example, $\bar{K}^*\pi^-$ waves) whereas in the Illinois approach the imaginary part of the appropriate density matrix elements cannot be directly determined without imposing constraints on the density matrix. (In the analogous $\pi^-\pi^-\pi^+$ system, the presence of a given isobar in two crossing bands in the Dalitz plot makes possible the determination of the imaginary part of the density matrix.)

The procedure in fitting the $K\pi\pi$ data is essentially the same as that employed in fitting the diffractive 3π data discussed fully in ref. 5. Table 3 lists the partial-wave sets employed, as a function of $K\pi\pi$ mass. The notation is $J^P L M^\eta$, followed by the isobar and odd particle. The quantities J^P refer to the angular momentum and parity of the state, L is the orbital angular momentum of the odd particle. The quantities M^η give the magnetic substates of the $K\pi\pi$ system, η being determined (at high energies) by the naturality of the exchange [14]: only waves with $\eta = +1$, corresponding to natural spin-parity exchange, were necessary.

The amplitudes for the isobars were taken as Breit-Wigner amplitudes for the $K^*(890)$, ρ, $K^*(1430)$, and f mesons. The ε amplitude was taken as proportional to the S-wave $I = 0$ $\pi\pi$ scattering amplitude ("down" solution [15]), and the κ amplitude was taken as an S-wave Breit-Wigner with a mass of 1.25 GeV and a width of 600 MeV *).

In the low-mass region, $1.0 \leq M_{K\pi\pi} \leq 1.6$ GeV, the data were binned in 20 MeV mass intervals for two regions of t', $0 \leq |t'| < 0.05$ GeV^2 and $0.05 \leq |t'| \leq 0.7$ GeV^2. In the high-mass region, all data in the interval $0 \leq |t'| \leq 0.7$ GeV^2 were fitted in 20 MeV mass bins.

The $K\omega$ data have not been subjected to partial-wave analysis, but the one-dimensional angular distributions have been found to be in excellent agreement with predictions from $K\rho$ amplitudes extracted from partial-wave analysis of the $K\pi\pi$ data (see Section 3.3). The effect of ρ-ω interference has not been included in the amplitude for the P-wave $\pi^+\pi^-$ isobar. The effect of including ρ-ω interference was studied in two mass bins at the peak of the $K\rho$ intensity and found to have no significant effect on any of the fitted amplitudes.

An overview of the data is provided in fig. 11, which shows the total intensity in each J^P state as a function of $K\pi\pi$ mass. The 1^+ system is dominant at low mass and has a strong peak at the lower Q resonance, with the upper Q appearing as a shoulder on the high-mass side. The 0^- intensity has a broad peak at $\sim$ 1.4 GeV, while 2^- peaks just below 1.8 GeV. A curious feature, which is unexplained, is

*) The $I = 0$ $K\pi$ S-wave phase shift passes slowly upward through 90° somewhere near 1.3 GeV. Beyond 1.4 GeV the amplitude decreases rapidly but is not very well determined [15].

the small peak in the 2^- intensity at $\sim$ 1.2 GeV: a similar effect was noted in the diffractive production of 3π, but only in the interval $0.3 \leq |t'| \leq 0.7$ GeV^2. The $K^*(1430)$ is picked out very clearly in 2^+, although the peak intensity is only $\sim$ 1000 events/20 MeV ($\sim$ 7% of the total intensity). A cross-section of 1 μb corresponds to 1430 ± 70 events (in fig. 11 and subsequent figures, one event represents 0.7 nb).

The total cross-section at 63 GeV for the reaction $K^-p \to K^-\pi^-\pi^+p$ between threshold and 2.1 GeV is 250 ± 12 μb. In the Q region the total cross-section is a slowly falling function of laboratory momentum (see fig. 12).

3. THE LOW-MASS REGION: 1.0-1.6 GeV

3.1 Introduction

The mass region 1.0-1.6 GeV has been analysed in two bins of t': $0 \leq |t'| < 0.05$ GeV^2 and $0.05 \leq |t'| \leq 0.7$ GeV^2. The only flip waves necessary were $1^+0^+(\rho K)$ and $1^+1^+(\rho K)$, with intensity $\lesssim$ 30% of the corresponding non-flip states. All partial waves in the low-mass region were found to be highly coherent, and the results are free from ambiguity. The only difficulty encountered was an inability to distinguish between the two 0^-S amplitudes, $0^-S(\kappa\pi)$ and $0^-S(\varepsilon K)$. While the total 0^- intensity was stable, individually $0^-S(\kappa\pi)$ and $0^-S(\varepsilon K)$ fluctuated wildly, with interference between the two maintaining the well-determined 0^- intensity. This effect is not surprising in view of the great similarity of the two amplitudes. The 0^-S amplitudes were therefore represented in the final wave set by only $0^-S(\varepsilon K)$. This was the more important of the two on the average, and the decrease in likelihood on removing a single 0^-S wave was less when $0^-S(\kappa\pi)$ was removed.

3.2 $J^P = 1^+$ waves: the Q mesons

The 1^+ system is observed in five separate $K\pi\pi$ channels in M = 0: $1^+S(K^*\pi)$, $1^+D(K^*\pi)$, $1^+S(\rho K)$, $1^+P(\kappa\pi)$ and $1^+P(\varepsilon K)$. The intensity in each channel, together with the phase of the corresponding amplitude, measured relative to $1^+S0^+(K^*\pi)$, is shown in fig. 13 for $0 \leq |t'| \leq 0.05$ GeV^2 and in fig. 14 for $0.05 \leq |t'| \leq 0.7$ GeV^2.

In the low $|t'|$ region, $0 \leq |t'| < 0.05$ GeV^2, the M = 1 amplitudes are very small and poorly determined, while for $0.05 \leq |t'| \leq 0.7$ GeV the M = 1 amplitudes $1^+S1^+(K^*\pi)$ and $1^+S1^+(\rho K)$ are important in the lower half of the Q enhancement and are well determined (fig. 15). The total intensity in $1^+S1^+(\rho K)$ is approximately half that in $1^+S0^+(\rho K)$, whereas the total intensity in $1^+S1^+(K^*\pi)$ is only ~ 0.1 of that in the lower half of $1^+S0^+(K^*\pi)$.

The M = 0 $K^*\pi$ intensity shows two clear peaks, at 1.25 and 1.4 GeV, while only the lower peak appears in M = 1. The relative height of the two M = 0 peaks changes in going from low t to higher t, reflecting the steeper t dependence of the low-mass region. The ρK channel shows a single peak at 1.3 GeV in both M = 0 and M = 1, with a phase which initially rises through $\sim 60°$ with respect to $1^+S0^+(K^*\pi)$ and then falls by a comparable amount between 1.35 and 1.45 GeV. These data at an energy of 63 GeV exhibit the features of the 13 GeV SLAC data [1], which have been attributed to diffractive production of two resonances. The $K\pi$ intensity and phase show the same features as the ρK channel, while the weak εK channel is qualitatively similar to $K^*\pi$. These features of the 1^+P0^+ waves have been observed before [16] but not reported in any detail.

The $1^+D(K^*\pi)$ amplitude has not been extracted in any previous study. The intensity has a single peak, and the phase relative to $1^+S(K^*\pi)$ moves forward through $\sim 80°$ before returning to the original value, as $M_{K\pi\pi}$ goes from 1.2 to 1.6 GeV.

All these features of the data are well represented in terms of a model in which two 1^+ resonances are produced diffractively, both directly and through rescattering of Deck backgrounds. The model is similar to the one mentioned in ref. 2, and has been used in the interpretation of diffractive 3π data in both one-resonance one-channel [5,7] and two-resonance four-channel versions [5,8]. For the analysis of the $K\pi\pi$ data, a version with two resonances and six channels was used, with the five observed $K\pi\pi$ channels fitted and the sixth channel, $K\omega$, unfitted but allotted couplings equal to $\sqrt{1/3}$ of the ρK couplings, as expected from the quark model with ideal ω-ϕ mixing.

The production amplitudes are given by

$$\underset{\sim}{F} = (\underset{\sim}{1} - i\underset{\sim}{\underset{\sim}{K}}\underset{\sim}{\rho})^{-1}\underset{\sim}{P} , \tag{3.1}$$

where the K-matrix has terms

$$K_{ij} = \frac{f_{ai}f_{aj}}{M_a - M} + \frac{f_{bi}f_{bj}}{M_b - M} . \tag{3.2}$$

The production vector P is given by

$$\underset{\sim}{P} = (\underset{\sim}{1} + \alpha\underset{\sim}{\underset{\sim}{K}})\underset{\sim}{D} + \underset{\sim}{R} , \tag{3.3}$$

where $\underset{\sim}{D}$ is a vector containing the Deck amplitudes in each channel and $\underset{\sim}{R}$ contains the direct production terms

$$R_i = \frac{f_{pa}f_{ai}}{M_a - M} + \frac{f_{pb}f_{bi}}{M_b - M} . \tag{3.4}$$

The constant α was taken as 0.4 as in ref. 5; the fits were not sensitive to the value of α.

The diagonal matrix $\underset{\sim}{\rho}$ contains the phase-space terms, taken as two-particle phase space evaluated at the complex mass of the isobar. The Deck amplitudes were calculated for π or K exchange, using the model described in ref. 5, except for the $1^+D(K^*\pi)$ channel where no Deck amplitude was included. The P-wave and D-wave centrifugal barrier factors were included in the Q-decay couplings f_{ai} and f_{bi} where appropriate, and the Deck amplitudes used were obtained by averaging the square of the amplitude over the K$\pi\pi$ Dalitz plot. The over-all phase was defined by taking f_{pa} real, and f_{pb} and the individual Deck amplitudes were allotted phases relative to f_{pa}.

The amplitudes (3.1) were fitted to the intensity of the five M = 0 K$\pi\pi$ channels, together with the phases measured relative to $1^+S0^+(K^*\pi)$, in the lower $|t'|$ bin, and to both M = 0 and M = 1 channels in the higher $|t'|$ bin. Although the model yields the relative 1^+ phases, only the variation of the 1^+ phases was fitted, the over-all phase of each channel being allowed to float by including an offset phase among the fitting parameters. This allows for any mismatch between reality and the assumptions made in either the partial-wave analysis or in the

fitting amplitudes: such an offset phase was found necessary when comparing the $2^+D(K^*\pi)$ and $2^+D(\rho K)$ amplitudes in the $K^*(1430)$ (see Section 3.4). These offset phases were negligible between $1^+S(K^*\pi)$ and $1^+D(K^*\pi)$, $\sim 30°$ between $K^*\pi$ and ρK, but $\sim 90°$ between the 1^+P waves and $K^*\pi$. Their inclusion does not affect any of the conclusions of this paper.

The results of fitting are shown in figs. 13-15, and the model represents the data very well. The fits shown in fig. 13 are to 215 data points with 26 parameters, and have a χ^2 of 529. The fits shown in figs. 14 and 15 are to 315 data points with 35 parameters and have a χ^2 of 1251. The only systematic discrepancy is found in $1^+S1^+(K^*\pi)$ where the model peaks 20 MeV above the data. When only $1^+S(K^*\pi)$ was fitted, using a two-resonance model with only one channel, both the M = 0 and the M = 1 data were very well represented, but the lower resonance had a mass 35 MeV below the value found when other channels are included. This difficulty has been found previously: the model used in ref. 2 produced a peak 50 MeV above the peak in those data.

It will be observed that the fit does not reproduce the full height of the sharp peak in $1^+S0^+(K^*\pi)$ for $0.05 \leq |t'| \leq 0.7$ GeV^2. This is not intrinsic to the model. On artificially reducing the errors on the two-peak data points, the fitted curve did reproduce the peak, without any significant shift of the parameters and without the fit going bad in any particular region. The χ^2 increased from 1251 to 1321. The failure of the fit shown to reproduce the peak is simply due to the negligible leverage exerted by any two or three data points.

The $K^*\pi$ M = 0 intensity is dominated by the upper resonance Q_a in conjunction with Deck background, although the lower resonance does decay into $K^*\pi$. The ρK and $K\pi$ M = 0 intensities are dominated by the lower resonance Q_b *). The masses and widths of these resonances are well determined (see table 4):

$$M_{Q_a} = 1.41 \pm 0.025 \text{ GeV}, \quad \Gamma_{Q_a} = 195 \pm 25 \text{ MeV},$$

$$M_{Q_b} = 1.27 \pm 0.01 \text{ GeV}, \quad \Gamma_{Q_b} = 90 \pm 8 \text{ MeV},$$

*) The labels a,b refer to the composition of the resonances, see eq. (3.5). The lower mass resonance is frequently labelled Q_1 and the upper Q_2.

where the errors are dominated by the estimated systematic uncertainties. These masses and widths have been obtained by calculating intensities in the $K^*\pi$ channel for production of only one resonance with no background, using the fitted parameters for that resonance. The resonance masses do not have the same value as the K-matrix poles because of the complex phase space used in (3.1), but because the two resonances couple predominantly to different channels, an elaborate search for second sheet poles of the T matrix is not necessary.

The ρK mass spectrum from production of Q_b alone is distorted because of the proximity of the woolly ρK threshold, and the resonance shape is markedly asymmetric. The full width of this asymmetric shape, measured at half peak height, is $\sim$ 120 MeV rather than 90 MeV.

The masses are in good agreement with values previously extracted. The total width of the lower resonance Q_b is half that obtained from analysis of the SLAC data [2], and the widths of both resonances are in good agreement with values obtained from non-diffractive Q production [17,18].

Diffractive production of two 1^+ resonances, close in mass, suggests that the two physical resonances Q_a and Q_b are mixtures of the two SU(3) octet states Q_A (C = +1 octet) and Q_B (C = -1 octet). The couplings to the vector-pseudoscalar channels may be explained in the same terms, for if

$$\begin{aligned} |Q_a\rangle &= |Q_A\rangle \cos\theta + |Q_B\rangle \sin\theta \\ |Q_b\rangle &= -|Q_A\rangle \sin\theta + |Q_B\rangle \cos\theta \ , \end{aligned} \tag{3.5}$$

then it is expected that [2,19]

$$\begin{aligned} f_{a1} &= \frac{1}{2}\gamma_+ \cos\theta + \sqrt{\frac{9}{20}}\gamma_- \sin\theta \\ f_{b1} &= -\frac{1}{2}\gamma_+ \sin\theta + \sqrt{\frac{9}{20}}\gamma_- \cos\theta \\ f_{a2} &= \frac{1}{2}\gamma_+ \cos\theta - \sqrt{\frac{9}{20}}\gamma_- \sin\theta \\ f_{b2} &= -\frac{1}{2}\gamma_+ \sin\theta - \sqrt{\frac{9}{20}}\gamma_- \cos\theta \ , \end{aligned} \tag{3.6}$$

where channel 1 is $K^*\pi$ and channel 2 ρK, with γ_+ and γ_- the reduced SU(3) couplings for Q_A (F-type) and Q_B (D-type), respectively. The couplings to S-wave $K^*\pi$ and ρK were therefore represented in terms of the three variables γ_+, γ_-, and θ, rather than four independent couplings. The production mechanism was not SU(3) constrained, and constraints were not imposed on the couplings to D-wave $K^*\pi$, $\kappa\pi$, and εK. The final values of the parameters are summarized in table 4.

The most elegant solution would be to have $\theta = 45°$ and $\gamma_+ = \sqrt{(9/5)}\gamma_-$, when the lower resonance would decouple completely from $K^*\pi$ and the upper from ρK. This scheme is not realized, the mixing angle being $\theta = 56° \pm 3°$ as determined from the couplings to the $K^*\pi$ and ρK channels. Further evidence for a mixing angle in excess of 45° comes from the direct production terms. If diffractive production proceeded via exchange of a C = +1 object, only the Q_A would be produced, and the production terms would be related by

$$f_{Pb} = -\tan\theta \, f_{Pa} \, .$$

The two M = 0 production amplitudes are indeed approximately 180° out of phase, and the ratio (see table 4) corresponds to a mixing angle $\sim 65°$. However, this pattern breaks down completely in M = 1, where the direct production amplitude for Q_b is about eight times that for Q_a. Dominance of Q_b in M = 1 is a feature which is not understood but has survived unchanged from 13 GeV [1,20] to 63 GeV [21,22] (see fig. 12) and must be attributed to the diffractive process.

The Q mixing angle obtained from these data is somewhat larger than the value $\sim 50°$ obtained from the SLAC data at 13 GeV [2,16]. (However, when only $K^*\pi$ and ρK channels are fitted, as in ref. 2, a value of 51° is obtained.)

The ratio of the direct production terms for Q_a and Q_b does not change on passing from the lower-t to the higher-t region. The change in t slope with $K\pi\pi$ mass may therefore be attributed to the slope-mass correlation obtaining in the Deck amplitudes (see table 4).

The data obtained in this experiment clearly require the existence of two diffractively produced 1^+ Q mesons. The principal features of the SLAC experiment [1] at 13 GeV have been confirmed, with a much larger sample of data. The major

differences obtained here are a much narrower width for the Q_b, a branching ratio $Q_b \to K\pi/Q_b \to \rho K$ a factor of 2 greater than was found in the SLAC experiment [16], and a slightly greater Q mixing angle. The hitherto unobserved $1^+D0^+(K^*\pi)$ channel has provided a nice confirmation of what has become the standard model of the Q region.

Detailed discussion of the Q parameters and an analysis of the status of the two 1^+ nonets expected on the basis of the quark model, are deferred to Section 5.

3.3 The ωK final state

There are only 2025 ωK events, and half of these lie in the Q region. The data have not been subjected to partial-wave analysis. Instead, the assumption has been made that the ωK amplitude is proportional to the ρK amplitude, the ρK amplitude being extracted from the $K\pi\pi$ data used to predict the properties of the ωK system. If it is assumed that a meson consisting only of strange quarks does not couple to two non-strange mesons, and that the ω-ϕ mixing is ideal so that the ω contains no strange quarks, then the amplitude for $Q^- \to \omega K^-$ is equal to the amplitude for $Q^- \to \rho^0 K^-$. The ωK^- and $\rho^0 K^-$ intensities will then differ only because of different phase-space factors.

The acceptance was calculated for each $K\omega$ mass bin by assuming that the ωK amplitudes are proportional to the ρK amplitudes. These amplitudes were used to generate Monte Carlo $K\omega$ events, which were then accepted or rejected according to the criteria applied to the real events. In addition to the criteria applied to the charged particles, the effects of the calorimeter on the additional π^0 were included (see Section 2.6). The over-all acceptance is $\sim$ 9% and is slowly varying with ωK mass.

The ωK mass spectrum is compared in fig. 16 with the mass spectrum predicted from the total $\rho^0 K$ mass spectrum. In addition to the correction for acceptance, the ωK spectrum has been corrected for decay modes other than $\omega \to \pi^+\pi^-\pi^0$, and a further factor of 1.9 is included because the $K\omega$ data were drawn from only the second half of the data-taking period. The very rapid rise from ωK threshold shows that the ωK channel couples to the lower Q, and the good agreement between

the shapes in the Q region shows that ωK does not have a substantial coupling to the upper Q. The data are in agreement with the assumption that the ωK amplitude is proportional to the ρK amplitude in the Q region. It is worth noting that the over-all $\pi^+\pi^-$ mass spectrum, after deleting events in K^* and $K^*(1430)$ bands, shows clear evidence for ρ-ω interference and is well fitted with the assumption that the ρ^0 and ω amplitudes are equal, when interference is taken into account by multiplying the ρ^0 amplitude by a factor $1 + \{\delta/[M_\omega - M_{\pi\pi} - i(\Gamma/2)\omega]\}$, with $\delta = 2.5$ MeV.

The one-dimensional angular distributions of the ωK system, using the normal to the ω decay plane as an analyser, have also been compared with the corresponding ρK angular distributions. The agreement is in all cases very good. In fig. 16 the angle χ between the incident K^- direction and the normal to the plane containing the K and the normal to the $\pi^+\pi^-\pi^0$ plane is seen to be distributed as $\sin^2\chi$, showing that for this sample the dominant wave is indeed $1^+S0^+(\omega K)$.

These results disprove a claim that the lower Q resonance is weakly coupled to ωK [18(b)]. The coupling is as expected from the ρK coupling and the quark model. A similar conclusion was reached in ref. 10.

3.4 $J^P = 2^+$ waves: $K^*(1430)$

The 2^+ intensity has been shown in fig. 11, and constitutes at peak less than 10% of the total intensity. Nonetheless it proved possible to obtain both the $2^+D1^+(K^*\pi)$ and $2^+D1^+(\rho K)$ intensities, and phases measured relative to $1^+S0^+(K^*\pi)$; the results are shown in fig. 17. The intensities obtained from the partial-wave analysis only become unstable for $2^+D1^+(K^*\pi)$ below $\sim$ 1.3 GeV, where the $2^+D1^+(K^*\pi)$ intensity is $\lesssim$ 2% of the total intensity.

The phase of $2^+D1^+(K^*\pi)$ increases relative to $1^+S0^+(K^*\pi)$ through $\sim 90°$ between 1.2 and 1.7 GeV, rather than through $\sim 180°$. A slow variation of phase is also exhibited by $2^+D1^+(\rho K)$. The fitted $1^+S0^+(K^*\pi)$ phase increases through $\sim 110°$ in this region (see fig. 14). Thus the slow variation of the 2^+ phases confirms this forward movement of the $1^+S0^+(K^*\pi)$ reference phase. In diffractive production of

3π, the slow forward movement of $2^+D1^+(\rho\pi)$ relative to $1^+S0^+(\rho\pi)$ established the substantial variation of phase in the latter [5,7].

There is a phase difference $\sim 30°$ between the $2^+D1^+(K^*\pi)$ and $2^+D1^+(\rho K)$ amplitudes. Such a difference should not be present if the 2^+ amplitudes are wholly resonant; so, in fitting to the data, an offset phase between the two was included. Fits were made with a model containing one resonance, coupled to four channels: $K^*\pi$, ρK, ωK (not fitted), and $K\pi$ (unobserved in this experiment). No background was included in the model. Since the K^* and ρ are in the same octet, the SU(3) relation between the couplings to the first two channels was imposed and the model fitted to the $2^+D1^+(K^*\pi)$ and $2^+D1^+(\rho K)$ data. The phase of the reference wave, $1^+S0^+(K^*\pi)$, obtained from fitting to 1^+ alone (fig. 14), was subtracted from the model 2^+ phases, and the variation of the resulting relative phase with $K\pi\pi$ mass was fitted to the observed relative phases simultaneously with fits to the intensities. The data are consistent with the SU(3) constraint, which predicts a branching ratio $\rho K/K^*\pi$ equal to 0.43, to be compared with the directly measured result $0.39 \pm \sim 0.03$, and the fit for the $K^*(1430)$ yields the following parameters:

$$M_{K^*(1430)} = 1.43 \text{ GeV}$$

$$\Gamma_{K^*(1430)} = 110 \text{ MeV} .$$

These values are in excellent agreement with the results of partial-wave analysis of a very large sample of $K\pi$ data [23].

3.5 $J^P = 0^-$ waves: the first radial recurrence of the kaon

Three 0^- waves were included in the partial-wave analysis: $0^-P(K^*\pi)$, $0^-P(\rho K)$, and $0^-S(\varepsilon K)$. The latter represented both $0^-S(\varepsilon K)$ and any contribution from $0^-S(\kappa\pi)$. The total 0^- intensity (fig. 11) suggests the presence of a resonance at a mass ~ 1.4 GeV. The intensity in each wave, together with the phase measured relative to $1^+S0^+(K^*\pi)$, is shown in fig. 18 for $0 \leq |t'| \leq 0.7$ GeV^2. The data cannot be interpreted in terms of Deck amplitudes alone, nor in terms of resonance production alone, but suggest both processes as in A_1 and Q production. The curves in fig. 18 are the results of fitting with a model containing a single resonance

coupling to all three channels, produced directly and through rescattering of Deck amplitudes, represented in this case by the simple Stodolsky form [24]. The fits represent well the qualitative behaviour of the 0^- amplitudes, and these data constitute strong evidence for the existence of a diffractively produced 0^- meson with a mass $\sim$ 1.46 GeV and width $\sim$ 260 MeV. The fitted partial widths are

$$\Gamma_{K^*\pi} = 109 \text{ MeV} , \quad \Gamma_{\rho K} = 34 \text{ MeV} , \quad \Gamma_{\varepsilon K} = 117 \text{ MeV} .$$

This resonance must be the first radial recurrence of the kaon; evidence for its existence was first presented in ref. 25. There is also evidence for a broad $I = 1$ 0^- resonance diffractively produced in 3π [5] with a mass somewhere in the range 1.2-1.6 GeV, and for an $I = 0$ resonance in $\eta\pi\pi$ [26], with mass $\sim$ 1.275 GeV and width $\sim$ 70 MeV. A 0^- nonet, the first radial recurrence of the (π,K,η,η') nonet, is thus almost complete and is approximately degenerate in mass with the P-wave $q\bar{q}$ mesons.

4. THE HIGH-MASS REGION: 1.5-2.1 GeV

4.1 Introduction

The high-mass region was analysed in 20 MeV bins, $0 \leq |t'| \leq 0.7$ GeV^2. A minimal wave set, in which the waves used below 1.6 GeV were augmented primarily by $2^-P0^+(\rho K)$, $2^-S0^+(K^{**}\pi)$, and $2^-S0^+(fK)$, was employed (table 3). It proved much more difficult to obtain satisfactory fits in this high-mass region than in the Q region, the symptoms being both substantial incoherence and some instability of the fitted amplitudes from bin to bin. It was found that when $2^-S0^+(fK)$ was included in both non-flip and flip waves, the fitted intensities in these two incoherent amplitudes were roughly equal. The quality of the fits did not greatly deteriorate when the fK wave was included in non-flip alone, and the total fK intensity did not change significantly. The wave set finally used included $1^+P0^+(\varepsilon K)$ in both non-flip and flip: the latter wave contributed a massive peak at a mass $\sim$ 1.7 GeV, $\sim$ 30% of the total $K\pi\pi$ intensity. This amplitude must be compensating for some unidentified effect. There is no reason to believe that

$1^+P0^+(\varepsilon K)$ is produced predominantly in flip, and, on removing it from flip, the intensity was redistributed among various minor 1^+ waves rather than transferred to the non-flip εK amplitude.

The reasons for the difficulty in fitting include the lower statistics in the high-mass region, the greater number of amplitudes necessary, and the lack of overlap of resonance bands in the Dalitz plot (fig. 19). The last of these effects, in particular, is responsible for a number of relative phases being poorly determined in the high-mass data.

The qualitative properties of the principal waves are, however, free from ambiguity and independent of the choice of minor waves. The errors on intensity and relative phases shown in figs. 20 and 21 are statistical errors only and so do not reflect uncertainties due to the difficulties described above.

4.2 2^- waves: the L meson

The L enhancement at a mass $\sim$ 1.8 GeV has long been known to be dominated by $J^P = 2^-$. Two $J^P = 2^-$ strange mesons are expected in this region from the first D-wave $q\bar{q}$ configurations, and the existence of the 2^- A_3 meson has been confirmed in diffractive 3π production [5,8].

The 2^- $K\pi\pi$ system is found, in this experiment, to couple to $2^-S(K^{**}\pi)$, $2^-S(fK)$, and $2^-P(K^*\pi)$. [A signal in $2^-P(\rho K)$ is barely significant.] The intensities and phases of the three 2^- waves are shown in fig. 20. The reference wave for $2^-S(K^{**}\pi)$ is $1^+S0^+(\rho K)$, because the K^{**} and ρ bands cross in the Dalitz plot. The $2^-S(fK)$ and $2^-P(K^*\pi)$ phases are measured relative to $2^-S(K^{**}\pi)$, but are poorly determined because neither the f nor the K^* band crosses the K^{**} band. There is a broad peak in both $2^-S(K^{**}\pi)$ and $2^-P(K^*\pi)$ and a narrower peak in $2^-S(fK)$, rising sharply from the fK threshold. The phase of $2^-S(K^{**}\pi)$ increases relative to $1^+S(\rho K)$ through $\sim 150^\circ$ across the L region. These features establish the existence of at least one resonance in the L region.

The variation of the $2^-S(fK)$ phase with respect to $2^-S(K^{**}\pi)$, although poorly determined, is reminiscent of the variation of the $1^+S(\rho K)$ phase relative to

$1^+S(K^*\pi)$ in the Q region: it is possible that the L enhancement contains two diffractively produced 2^- mesons.

Fits have been made to these data with amplitudes containing Deck backgrounds and either one resonance (solid curves in fig. 20) or two resonances (broken curves in fig. 20). The fits with two resonances are slightly better, but it may only be concluded that the data demand at least one L meson and are consistent with two. The resonance parameters obtained from the two fits are summarized in table 5.

4.3 1^+ waves: another radial recurrence?

The various 1^+ amplitudes were sensitive to the choice of waves included in the partial-wave analysis. Three principal variants were tried: $2^-(fK)$ in non-flip only, with $1^+(\varepsilon K)$ included in flip and non-flip; $2^-(fK)$ and $1^+(\varepsilon K)$ in both flip and non-flip; no flip waves at all. The total 1^+ intensity was stable under these changes. The $1^+S(K^*\pi)$ was very small in all cases, and $1^+D(K^*\pi)$ exhibited a peak at $\sim$ 1.8 GeV, independent of the choice of waves. In the final set chosen, $1^+(\varepsilon K)$ is flip-dominated, giving a peak at $\sim$ 1.8 GeV containing $\sim$ 30% of the total intensity in this region. When $1^+(\varepsilon K)$ was removed from the flip waves, the intensity was redistributed over the other waves, particularly $1^+(\rho K)$ in flip when this was present.

The $1^+D(K^*\pi)$ intensity is shown in fig. 21a. The lower peak at $\sim$ 1.3 GeV fits very well into the framework of the standard Q model (Section 3.2), and the upper peak, at about 1.8 GeV, contains a comparable number of events. This upper peak has an analogue in diffractive production of 3π. The total $1^+(\varepsilon K)$ intensity is shown in fig. 21b, for the wave set finally chosen. The enhancement at 1.8 GeV dominates the two-peak structure in the Q region, but comes mostly from the flip waves.

These peaks in 1^+ waves, reflected in the total 1^+ intensity (which is stable under choice of wave set), suggest the existence of a further 1^+ resonance in the L region: a radial excitation of the Q's. Taken in conjunction with the 1^+D peak at $\sim$ 1.7 GeV in 3π and the good evidence for radial recurrences of the pseudoscalar

mesons degenerate with the lowest-lying 1^+ multiplets, these data suggest a picture of radial recurrences displaced downwards by one unit from the position expected for a simple harmonic oscillator potential between q and $\bar{q}$. The data on the second 1^+ peaks, in both 3π and $K\pi\pi$, are not however good enough to establish the existence of corresponding 1^+ mesons and may only be taken as indicative.

5. SU(3) STRUCTURE OF THE 1^+ MULTIPLETS

5.1 Introduction

The $q\bar{q}$ system with L = 1 gives rise to a triplet 2^+ nonet, a triplet 1^+ nonet and a singlet 1^+ nonet, and a triplet 0^+ nonet. The first 2^+ nonet (A_2, K**, f';f) has been established for a long time. Until 1975 the singlet 1^+ nonet was represented only by the B(1235), and the only possible representative of the triplet 1^+ nonet was the D(1275). The SLAC experiment [1] provided good evidence for the existence of two nearly degenerate strange 1^+ mesons -- mixtures of the C = +1 (triplet) and C = -1 (singlet) SU(3) octets -- a result confirmed by the present data. Recently, proof of the existence of the I = 1 triplet 1^+ A_1 meson has been obtained in diffractive production of 3π [5,7] and in charge exchange [27], and evidence for an isosinglet member of the singlet 1^+ nonet has been obtained in charge exchange [27]. The C = +1 property of the E(1425) has been confirmed [28,29] and $J^P = 1^+$ is now favoured [28]. The two 1^+ nonets predicted by the quark model are therefore nearly complete and there are sufficient data for examining how well these mesons fit into the quark model scheme. The agreement between the data and expectations based on the quark model is rather good: only the relatively large amplitude for $Q_b \to K\pi$ fails to fit into the scheme.

5.2 Disentangling the Q mesons

If the two Q mesons predicted by the quark model did not mix, then only the triplet Q would be strongly produced in diffractive processes, and both Q's would have a reduced branching ratio $K^*\pi/\rho K$ equal to unity, after removing phase-space effects. However, the upper Q couples overwhelmingly to $K^*\pi$, the lower to ρK and $K\pi$, and both are diffractively produced. The mixing between the two SU(3) octet

states was taken into account in fitting (as described in Section 3.2), which yielded, in addition to the masses of the physical (mixed) states Q_a and Q_b, the mixing angle θ determined from the $K^*\pi$ and ρK decay modes, and the reduced coupling constants γ_+ and γ_- which can be used to predict partial widths for other members of the nonets.

If the SU(3) breaking which mixes the states does not change the decay couplings, then

$$M_{Q_A} + M_{Q_B} = M_{Q_a} + M_{Q_b} \tag{5.1}$$

$$M_{Q_A} - M_{Q_B} = (M_{Q_a} - M_{Q_b}) \cos 2\theta \ ,$$

where M_{Q_A} and M_{Q_B} are the masses of Q_A (triplet) and Q_B (singlet), respectively.

If the mixing angle $\theta = 56° \pm 3°$, determined from the decay amplitudes, is used in eqs. (5.1), then the masses of the SU(3) states are

$$M_{Q_A} = 1.31 \pm 0.015 \text{ GeV} \ ,$$

$$M_{Q_B} = 1.37 \pm 0.02 \text{ GeV} \ .$$

The Q_B emerging is perhaps a little heavier than the Q_A, although the A_1 is probably heavier than the B meson.

5.3 The singlet (C = -1) nonet

The I = 1 B(1235) decays into $\omega\pi$ in both the S-wave and the D-wave. The SU(3) relations alone are insufficient for making a prediction of the width of B, because ω is a mixture of the 1^- octet and 1^- singlet. If it is assumed that the $\phi\pi$ is decoupled from B, then the S-wave partial width for $B \to \omega\pi$ is given by

$$\Gamma^S_{B\to\omega\pi} = \frac{6}{5} \gamma_-^2 \rho_{\omega\pi} \ ,$$

where $\rho_{\omega\pi}$ is $\omega\pi$ phase space, yielding a value of 118 ± 28 MeV. The D wave coupling can be extracted from the mixing angle θ and the Q_a and Q_b couplings to D-wave $K^*\pi$, yielding a D/S ratio for the B of 0.4 ± 0.1, and a partial width $\Gamma^D_{B\to\omega\pi} = 19 \pm 8$ MeV.

The total width of the B, calculated from the Q data, is 137 ± 30 MeV, and all these results are in excellent agreement with the measured properties of the B meson [15].

Evidence for an isoscalar member H of the singlet nonet has only recently been obtained [27]. The masses of B and Q_B may be used to obtain the mass of the SU(3) octet H using the Gell-Mann - Okubo formula, giving

$$M_{H8} \simeq 1.4 \text{ GeV} .$$

The value of γ_- (from either the Q data or the B width) then gives the octet member a width

$$\Gamma_{H8 \to \rho\pi} \simeq 120 \text{ MeV} .$$

If the SU(3) octet and SU(3) singlet members are ideally mixed, then it is to be supposed that $M_H \simeq M_B$, when

$$\Gamma_{H \to \rho\pi} = 3\Gamma_{B \to \omega\pi} .$$

An H meson with a mass $\sim$ 1.23 GeV and a width into $\rho\pi \sim$ 350 MeV is entirely consistent with the charge-exchange data of ref. 27. The corollary is the existence of an H′ meson composed only of strange quarks, with a mass

$$M_{H'} \simeq 1.48 \text{ GeV} .$$

The H′ would decay into $K^*\bar{K} + \bar{K}^*K$ with a width

$$\Gamma_{H'} \simeq 165 \text{ MeV} .$$

The discovery of this particle would complete the L = 1 singlet (C = −1) nonet.

5.4 The triplet (C = +1) nonet

There are now candidates for all members of the L = 1 triplet $q\bar{q}$ nonet: $A_1(\sim 1280)$, $Q_A(1320)$, D(1275), E(1420). The existence of the A_1 meson is now well established [5,7,27] although there remains some doubt about the precise value of the mass of this broad object. Analysis of diffractive production of 3π in terms of resonance production, Deck background, and rescattering, yields a value for the mass $M_{A_1} = 1.28 \pm 0.03$ GeV [5,7]. The charge-exchange data of ref. 27 have a broad peak at 1.15 GeV. The two sets of data can be reconciled by either including a multi-Regge background in the charge-exchange data, or adding an attractive background term in ρπ scattering. The A_1 pole is then found to be at a mass 1.23-1.28 GeV, depending on the detailed assumptions.

The width for $A_1 \to \rho\pi$ S-wave is given by

$$\Gamma^S_{A_1 \to \rho\pi} = \frac{4}{3} \gamma_+^2 \rho_{\rho\pi} , \tag{5.2}$$

where $\rho_{\rho\pi}$ is $\rho\pi$ phase space, which, using the value of γ_+ obtained from the Q data, yields

$$\Gamma^S_{A_1 \to \rho\pi} = 270 \pm 45 \text{ MeV}$$

at a mass of 1.28 GeV. The partial width into D-wave $\rho\pi$ can be extracted from the Q couplings to D-wave $K^*\pi$, yielding $\Gamma^D_{A_1 \to \rho\pi} < 10$ MeV. These results are in good agreement with the measured properties of the A_1.

The mass of the octet isoscalar member may be calculated, with the Gell-Mann - Okubo formula, from the mass of the A_1 and Q_A:

$$4M_{Q_A} = 3M_{8^+} + M_{A_1} \tag{5.3}$$

(it is immaterial whether the linear or quadratic version of this expression is used). If M_{A_1} is taken between 1.23 and 1.28 GeV, then M_{8^+} is between 1.35 and 1.33 GeV for $M_{Q_A} = 1.32$ GeV. If Q_A and Q_B are degenerate, then M_{8^+} lies between 1.38 and 1.36 GeV. Thus

$$M_{8^+} = 1.35 \pm \sim 0.03 \text{ GeV} ,$$

and since $M_{8^+} + M_{1^+} = M_D + M_E$ if D and E are members of this nonet,

$$M_{1^+} = 1.35 \pm \sim 0.03 \text{ GeV} .$$

These results place some constraint on the D-E mixing. If

$$\begin{aligned} |D\rangle &= \cos\xi |1^+\rangle + \sin\xi |8^+\rangle \\ |E\rangle &= -\sin\xi |1^+\rangle + \cos\xi |8^+\rangle , \end{aligned} \tag{5.4}$$

then

$$\cos 2\xi = \frac{M_{1^+} - M_{8^+}}{M_D - M_E} = \frac{0 \pm \sim 0.05}{-0.14} \tag{5.5}$$

so that

$$\xi = 45^\circ \pm \sim 10^\circ .$$

The lower limit corresponds to ideal mixing, which is also suggested by the approximate degeneracy of A_1 and D.

The partial width of the E into $K^*\bar{K} + \bar{K}^*K$ is given by

$$\Gamma_{E \to K^*K} = 2\gamma_+^2 \cos^2 \xi \rho_{K^*K}$$
$$= 80 \pm 15 \text{ MeV for ideal mixing}$$
$$= 60 \pm 10 \text{ MeV for } \xi = 45^\circ$$
$$= 40 \pm 7 \text{ MeV for } \xi = 55^\circ .$$

The measured width of the E is 40 ± 15 MeV, with a branching ratio into $K^*\bar{K} + \bar{K}^*K$ consistent with unity [28]. There is no convincing evidence for the decay $E \to \delta\pi$: in particular, there is no sign of an E signal above the D in the process [26]

$$\pi^- p \to \eta\pi\pi n ,$$

although both D and E are produced in the process [28]

$$\pi^- p \to K\bar{K}\pi n .$$

Thus the data on E decay into $K^*\bar{K} + \bar{K}^*K$ are entirely consistent with the E being a member of the triplet 1^+ nonet. This identification, however, suggests a mixing angle greater than 45°, the SU(3) singlet being heavier than the octet state.

5.5 A problem with the triplet (C = +1) nonet

The (physical) Q_b state has a branching ratio into $\kappa\pi \sim 30\%$, whereas the upper Q_a has a negligible coupling to this channel. The couplings of Q_A and Q_B to $\kappa\pi$ are therefore comparable and substantial, using the mixing formalism. The couplings of Q_A to $\kappa\pi$ may be determined using the Q mixing angle obtained from the $K^*\pi$ and ρK decay modes, and be used to predict the widths for the decays $D \to \delta\pi$ and $E \to \delta\pi$ under the assumption that κ and δ are members of the same SU(3) octet. The $\delta\pi$ phase space and kinematical barrier factors have approximately the same value for D and E decay. In this approximation, the sum of the partial widths into $\delta\pi$ for D and E is independent of the mixing angle ξ.

The value depends not only on SU(3) Clebsch-Gordan coefficients, but also on the quark composition of κ and δ. If it is supposed that κ and δ are members of a $q\bar{q}$ octet, then the $Q_b \to \kappa\pi$ coupling yields a prediction

$$\Gamma_{D\to\delta\pi} + \Gamma_{E\to\delta\pi} = 460 \pm 160 \text{ MeV} ,$$

whereas if κ and δ are members of a four-quark octet, the prediction is

$$\Gamma_{D\to\delta\pi} + \Gamma_{E\to\delta\pi} = 230 \pm 80 \text{ MeV} .$$

The four-quark model is probably ruled out because the decay $Q_B \to K\pi$ is forbidden if Q_B and π are two-quark states and κ is a four-quark state. Thus a conservative estimate of the sum of the D and E partial widths into $\delta\pi$ is

$$\Gamma_{D\to\delta\pi} + \Gamma_{E\to\delta\pi} > 150 \text{ MeV} ,$$

which is completely inconsistent with the measured total widths.

The $K\pi$ amplitude is important below 1.4 GeV, corresponding to $K\pi$ masses < 1.3 GeV. In this region the crude representation of the 0^+ $K\pi$ amplitude employed should be sufficiently accurate. The conclusion that the D/E width into $\delta\pi$ should be large is not strongly dependent on the kinematic factors used, and there seems no way of escaping this conclusion within simple SU(3) quark-model relations. Either the identification of the pair of states D(1275) and E(1420) with the $q\bar{q}$ L = 1 triplet isoscalar states is wrong, or else the SU(3) quark model relations do not work for the decays $Q \to K\pi$, D, $E \to \delta\pi$. (For example, κ and δ might be different mixtures of two-quark and four-quark states.)

5.6 Production characteristics of Q_a and Q_b

The SLAC experiment [1] revealed some curious characteristics of diffractive production of Q_a and Q_b: the steeper t slope in the production of M = 0 $K\pi\pi$ in the Q_b region; the dominance of Q_b in M = 1; and a significant component of C = -1 exchange in Q_a production. This experiment has confirmed the first two features, but provides no information on the third. The t-slope correlation with $K\pi\pi$ mass is explained in this analysis in terms of a correlation affecting the Deck background only, but in the model employed in this paper the direct production amplitudes for Q_b have a substantial M = 1 component, whereas Q_a is produced with relatively small M = 1 amplitudes.

A further curious feature is encountered in Q production by strangeness and charge exchange. In strangeness exchange only the Q_b is significantly produced [18],

whereas in charge exchange the Q_a dominates -- in natural spin-parity exchange [17]. Since Q_b approximately decouples from $K^*\pi$, and Q_a from ρK, these production characteristics seem the wrong way round.

6. CONCLUSIONS

The existence of two $J^P = 1^+$ diffractively produced Q mesons has been confirmed. These objects are mixtures of Q_A and Q_B, the unmixed states which are members of the A_1 and B octets. The couplings of Q_A and Q_B to vector-pseudoscalar are in excellent agreement with those found from the decay of A_1 and B, respectively.

The B, Q_B, and recently observed H [27] fit nicely into a nonet structure, the one missing member being an H′ with a mass $\sim$ 1.48 GeV and width into $K^*\bar{K} + \bar{K}^*K$ that is $\sim$ 165 MeV. The A_1, Q_A, D, and E make up a possible nonet although the isosinglet D and E may not be ideally mixed. The P-wave decay $Q_A \to K\pi$ however suggests a very large D/E width into $\delta\pi$, quite inconsistent with experiment.

The existence of a broad $0^-(K')$ resonance with a mass $\sim$ 1.46 GeV may now be taken as established: there is a nearly complete nonet of 0^- states approximately degenerate with the first 1^+ states.

The L region contains at least one 2^- meson, and there are indications of at least one more 1^+ state approximately degenerate with the 2^- object. A similar feature has been observed in diffractively produced 3π [5].

The reactions

$$K^-p \to K\bar{K}\pi\Lambda \ , \quad K^-p \to \eta\pi\pi\Lambda \ ,$$

seem particularly worthy of study in a high-statistics experiment in order to search for the H′ and further elucidate the nature and properties of the E meson.

REFERENCES

[1] G.W. Brandenburg et al., Phys. Rev. Lett. 36 (1976) 703 and 706; Nucl. Phys. B127 (1977) 509.

[2] M.G. Bowler, J. Phys. G3 (1977) 775.

[3] J.-L. Basdevant and E.L. Berger, Phys. Rev. 19 (1979) 246.

[4] R.T. Deck, Phys. Rev. Lett. 13 (1964) 169.

[5] C. Daum et al., Diffractive production of 3π states at 63 and 94 GeV, preprint CERN-EP/80-219 (1980), submitted to Nucl. Phys. B.

[6] C. Daum et al., Phys. Lett. 89B (1980) 276.

[7] C. Daum et al., Phys. Lett. 89B (1980) 281.

[8] C. Daum et al., Phys. Lett. 89B (1980) 285.

[9] G. Ascoli et al., Max-Planck Institute report MPI-PAE/Exp. E1. 77 (May 1979).

[10] G. Otter et al., preprint CERN-EP/80-17 (1980).

[11] D.J. Herndon et al., Phys. Rev. D 11 (1975) 3165; see also ref. 5.

[12] J.D. Hansen et al., Nucl. Phys. B81 (1974) 403; see also ref. 5.

[13] R.J. Cashmore, *in* Proc. Daresbury Study Weekend No. 8,1975 (eds. J.B. Dainton and A.J.G. Hey) (Sci. Research Council, Daresbury, 1975), p. 15.

[14] J.P. Ader et al., Nuovo Cimento 56A (1968) 952.

[15] Particle Data Group, Rev. Mod. Phys. 52, No. 2, Part II (1980).

[16] R.K. Carnegie et al., Phys. Lett. 68B (1977) 287.

[17] a) S.M. Vergeest et al., Phys. Lett. 62B (1976) 471.
b) W. Beusch et al., Phys. Lett. 74B (1978) 282.
c) K.J. Foley et al., Phys. Rev. D 22 (1980) 42.

[18] a) D.J. Crennell et al., Phys. Rev. D 6 (1972) 1220.
b) P. Gavillet et al., Phys. Lett. 76B (1978) 517.

[19] M.G. Bowler et al., Nucl. Phys. B74 (1974) 493.

[20] G. Otter et al., Nucl. Phys. B93 (1975) 365.

[21] S. Tovey et al., Nucl. Phys. B95 (1975) 109.

[22] Yu.M. Antipov et al., Nucl. Phys. B86 (1975) 381.

[23] P. Estabrooks et al., Nucl. Phys. B133 (1978) 490.

[24] L. Stodolsky, Phys. Rev. Lett. 18 (1967) 973.

[25] G. Brandenburg et al., Phys. Rev. Lett. 36 (1976) 1239.

[26] N.R. Stanton et al., Phys. Rev. Lett. 42 (1979) 346.

[27] J.A. Dankowych et al., Paper submitted to the 6th Int. Conf. on Experimental Meson Spectroscopy, Brookhaven, 1980.

[28] C. Dionisi et al., Nucl. Phys. B169 (1980) 1.

[29] D. Scharre, Stanford preprint SLAC-PUB-2519 (1980), invited talk given at the 6th Int. Conf. on Experimental Meson Spectroscopy, Brookhaven, 1980;
D. Scharre et al., Phys. Lett. 97B (1980) 329.

Table 1

Čerenkov identification: single-track assignments

The assignments of single tracks are given according to the condition of the appropriate Čerenkov cells. Those cases where a secondary could have "Any" assignment are marked A.
Assignments in parentheses correspond to less than 1% of all tracks.

Čerenkov state		Secondary momentum (GeV)				
		0-8	8-17.4	17.4-28	28-53	53-63
C1	C2					
OFF	OFF	A	K/p	K/p	p	(K/p)
OFF	ON	(π)	(π)	(π)	(π)	(π)
ON	OFF	(π)	π	π a)	K	K/p
ON	ON	(π)	(π)	π	π	(π)
C1 only						
OFF		A	K/p	K/p	(p)	(A)
ON		(π)	π	(π)	π/K	(A)
C2 only						
	OFF	(A)	A	K/p	K/p	K/p
	ON	(π)	(π)	π	π	(π)

a) In this class, those tracks with momentum between 27 and 28 GeV, close to nominal C1 threshold for kaons, were assigned as kaons.

Table 2

Čerenkov identification: Complete events assigned to Kππ

The final assignment of secondaries is given, event by event, to $K^-\pi^-\pi^+$ for combinations of the single-track assignments listed in Table 1. Also given is the number of events of each category, in percent (see text).

Final assignment											
K^-	π^-	π^+	%	K^-	π^-	π^+	%	K^-	π^-	π^+	%
K	A	π	6.0	p	K/π	π	0.0	K	A	A	6.3
K/p	A	π	16.4	p	π	π	1.2	K/p	A	A	6.5
K/p	K/π	π	0.1	p	π	A	1.6				
K	π	π	4.1	p	π	K/π	0.0				
K/p	π	π	20.7	p	A	π	1.3				
A	π	A	4.0	K/p	π	K/p	0.8				
K/π	π	A	0.8	K	π	K/p	0.3				
A	π	K/π	0.0	K	K/p	π	0.0				
K/π	π	K/π	0.0								
A	π	π	9.6								
K/π	π	π	0.4								
K	π	A	9.1								
K	π	K/π	0.0								
K/p	π	A	10.6								
K/p	π	K/π	0.1								
K	K/π	π	0.0								

Table 3

Final wave sets used in the partial-wave analysis *)

Mass range (GeV)	1.0-1.1	1.1-1.2	1.2-1.3	1.3-1.4	1.4-1.5	1.5-1.6	1.6-1.7	1.7-2.1
Non-flip waves	$0^-P0^+(K^*\pi)$	———	———	———	———	———	———	
	$1^+S0^+(K^*\pi)$	———	———	———	———	———	———	———
		$0^-S0^+(\varepsilon K)$	———	———	———	———	———	———
		$1^+P0^+(\varepsilon K)$	———	———	———	———	———	———
		$1^+P0^+(\kappa\pi)$	———	———	———	———	———	———
		$1^+S0^+(\rho K)$	———	———	———	———	———	———
		$1^+S1^+(K^*\pi)$	———	———	———	———	———	———
		$1^+S1^+(\rho K)$	———	———	———	———	———	
		$2^+D1^+(K^*\pi)$	———	———	———	———	———	
		$2^-P1^+(K^*\pi)$	———	———	———	———	———	———
			$0^-P0^+(\rho K)$	———	———	———	———	———
			$1^+D0^+(K^*\pi)$	———	———	———	———	———
			$1^+P1^+(\kappa\pi)$	———				
				$2^+D1^+(\rho K)$	———	———	———	
							$1^+D0^+(\rho K)$	
							$2^-P0^+(\rho K)$	———
						$2^-S0^+(K^{**}\pi)$	———	———
							$2^-S0^+(fK)$	———
Flip waves		$1^+S0^+(\rho K)$	———	———	———	———	———	———
		$1^+S1^+(\rho K)$	———	———	———	———	———	———
							$1^+P0^+(\varepsilon K)$	———

*) Each wave is entered in the column where it was first included: the bar shows the range.

Table 4

Properties of the Q mesons

Table 4a

	K-matrix poles		Vector-pseudoscalar couplings			M = 0 direct production terms			Coeff. of M = 0 $K^*\pi$ Deck amplitude
	M_a	M_b	γ_+	γ_-	θ (°)	fp_a	fp_b	Phase of fp_b (°)	
Low-t data	1.40 ± 0.02	1.17 ± 0.02	0.78 ± 0.1	0.54 ± 0.1	64 ± 8	11	-26	29 ± 47	1.78
High-t data	1.40 ± 0.02	1.15 ± 0.03	0.86 ± 0.1	0.63 ± 0.08	54 ± 4	16	-37	24 ± 31	1.58
			Average						
			0.82 ± 0.07	0.59 ± 0.07	57 ± 3				

Table 4b

	M_{Q_a} (GeV)	Γ_a (MeV)	Branching ratios Q_a $K^*\pi$(S)	$K^*\pi$(D)	ρK	ωK	$\kappa\pi$	εK
Low-t data	1.41 ± 0.025	165 ± 35	0.87 ± 0.05	0.03 ± 0.005	0.05 ± 0.04	0.01 ± 0.01	∼0	0.02 ± 0.02
High-t data	1.41 ± 0.025	225 ± 25	0.93 ± 0.03	0.04 ± 0.01	0.01 ± 0.01	∼ 0.002	∼0	0.01 ± 0.01

	M_{Q_b} (GeV)	Γ_b (MeV)	Branching ratios Q_b $K^*\pi$(S)	$K^*\pi$(D)	ρK	ωK	$\kappa\pi$	εK
Low-t data	1.27 ± 0.007	90 ± 8	0.13 ± 0.03	0.07 ± 0.006	0.39 ± 0.04	0.10 ± 0.01	0.29 ± 0.02	0.02 ± 0.005
High-t data	1.274 ± 0.012	90 ± 8	0.03 ± 0.01	0.08 ± 0.01	0.46 ± 0.04	0.12 ± 0.01	0.27 ± 0.03	0.04 ± 0.01

Table 4a lists the values of some important fitting parameters. The ratio fp_a to fp_b is the same for both low-t and high-t data, and the coefficients of the M=0 $K^*\pi$ t-averaged Deck amplitudes are close. These features show that the t-slope-mass correlation may be attributed to the Deck background.

Table 4b lists the masses, widths and branching ratios of the Q mesons. Decay into charge states other than $K^-\pi^-\pi^+$ has been taken into account in calculating the branching ratios. Purely statistical errors are much smaller than systematic uncertainties; these are taken from the range of values for which acceptable fits are obtained and from the spread of values found when fitting different selections of data and with minor variants of the model.

Table 5

L resonance parameters

	Mass (GeV)	Width (MeV)	Approximate branching ratios		
			$K^{**}\pi$	fK	$K^{*}\pi$
One resonance	1.82	$\sim$ 200	0.6	0.16	0.24
Two resonances	1.78	$\sim$ 210	0.03	0.74	0.23
	1.84	$\sim$ 230	0.77	0.18	0.05

Figure captions

Fig. 1 : Plan view of the spectrometer, showing the photon calorimeter (c) at the downstream end.

Fig. 2 : The figure shows the over-all construction of the photon calorimeter, together with a detail. Each fork had 20 prongs of scintillator.

Fig. 3 : Response R of the threshold Čerenkov counters as a function of secondary momentum, for kaon primaries. R is the ratio of the number of tracks giving Čerenkov light to the total number; the nominal π and K thresholds are indicated.

Fig. 4 : Results using calorimeter data to identify Kω events:

a) $\gamma\gamma$ mass spectrum from all events containing at least two γs;

b) $\pi^+\pi^-\pi^0$ mass spectrum, the π^0 being selected using the cuts shown in (a);

c) visible longitudinal momentum spectrum of the $K^-\pi^-\pi^+\pi^0$ system, showing cuts applied to remove extra unseen particles;

d) $\pi^+\pi^-\pi^0$ mass spectrum after applying the cuts shown (c), showing cuts applied to select $\omega \to \pi^+\pi^-\pi^0$.

Fig. 5 : a) $\pi^+\pi^-$ mass spectrum from $\bar{K}^0$ decay;

b) $\pi^-\pi^-\pi^+$ mass spectrum from the τ decay mode of K^-;

c) missing mass squared recoiling against the $K^-\pi^-\pi^+$ system.

Fig. 6 : The $K^-\pi^+$ and $\pi^-\pi^+$ mass spectra (raw data). The $K^-\pi^+$ system is dominated by $K^*(890)$, but $K^*(1430)$ is clearly visible. The ρ is seen in $\pi^+\pi^-$, with a low-mass shoulder which is the reflection of the $K^*(890)$. The f meson contributes a shoulder above 1.2 GeV.

Fig. 7 : Acceptance of the apparatus for $K^-\pi^-\pi^+$ as a function of both K$\pi\pi$ mass and four-momentum transfer squared to the proton, t'. The trigger acceptance includes both geometrical factors and the effects of secondary interactions and decay. The acceptance after all cuts includes the effects of demanding event identification and the effect of the F counter condition imposed off line.

Fig. 8 : The $K^-\pi^-\pi^+$ mass spectrum, $0 \leq |t'| \leq 0.7$ GeV^2 (raw data). The two-peak structure of the massive Q enhancement is clear, and the L enhancement contributes above 1.6 GeV. The raw Kω mass spectrum is shown as an insert, with a very rapid rise from threshold in the Q region.

Fig. 9 : The distribution in four-momentum transfer squared to the proton, t' ($= t - t_{min}$) for two regions of K$\pi\pi$ mass:

a) $1.2 \leq M_{K\pi\pi} < 1.35$ GeV

b) $1.35 \leq M_{K\pi\pi} \leq 1.45$ GeV (raw data). The slope is steeper for the lower mass region, and in both cases flattens beyond $|t'| =$ $= 0.4$ GeV^2. The initial slopes are approximately 12 and 10 GeV^{-2}, respectively.

Fig. 10 : The correlation between K$\pi\pi$ mass and the slope parameter B in the expression $d\sigma/dt = Ne^{Bt}$, fitted to the $K^-\pi^-\pi^+$ intensity in the range $0 \leq |t'| \leq 0.4$ GeV^2.

Fig. 11 : The total intensities in 1^+, 0^-, 2^+ and 2^-, $0 \leq |t'| \leq 0.7$ GeV^2, are shown on the same scale for the full mass region analysed.

Fig. 12 : Variation of $K^-\pi^-\pi^+$ cross-section in the Q region as a function of laboratory momentum of the incoming beam, p_{lab}. The total cross-section data, $1.2 \leq M_{K\pi\pi} \leq 1.6$ GeV, have been extracted from ref. 1 for 13 GeV and taken from refs. 21 (14.3 GeV) and 22 (25 and 40 GeV). The partial cross-sections at 13 GeV have been extracted from ref. 1. All cross-sections fall slowly with p_{lab}: note that the ratio of $1^+S1^+(\rho K)$ to $1^+S0^+(\rho K)$ does not significantly change between 13 and 63 GeV. The values plotted for 63 GeV are 155 ± 8 μb, 77 ± 7 μb, 15 ± 2 μb and 7 ± 1 μb.

Fig. 13 : Results of partial-wave analysis in the Q region, $1.0 \leq M_{K\pi\pi} <$ ≤ 1.6 GeV, for 1^+0^+ waves, $0 \leq |t'| < 0.05$ GeV^2. The phases are measured with respect to $1^+S0^+(K^*\pi)$ and the curves show the fits obtained with two Q resonances and coherent background. The calculated $1^+S0^+(K^*\pi)$ phase variation is also shown.

Fig. 14 : Results of partial-wave analysis in the Q region for 1^+0^+ waves, $0.05 \leq |t'| \leq 0.7$ GeV^2 (see caption to fig. 13).

Fig. 15 : Results of partial-wave analysis in the Q region for 1^+1^+ waves, $0.05 \leq |t'| \leq 0.7$ GeV^2. The phases are measured relative to $1^+S0^+(K^*\pi)$ and the curves show the fits obtained when fitting together with the data of fig. 14.

Fig. 16 : a) The ωK mass spectrum at production is compared with the spectrum predicted on the assumption that the ωK amplitudes are equal to the $\rho^0 K$ amplitudes. The ωK data have been corrected for acceptance, for ω decays other than $\pi^+\pi^-\pi^0$, and finally multiplied by a factor 1.9 to account for the shorter period of data taking with the photon calorimeter installed.

b) Distribution of the angle χ (see text) for $M_{\omega K} < 1.4$ GeV, $|t'| < 0.05$ GeV^2. For the equivalent selection, the ρK amplitude is predominantly 1^+0^+S wave and for $1^+S0^+(\omega K)$ the angle χ should be distributed according to $\sin^2 \chi$ (solid curve). Raw data: the acceptance is a slowly varying function of χ for this selection.

Fig. 17 : Intensities and phases measured relative to $1^+S0^+(K^*\pi)$ of the waves $2^+D1^+(K^*\pi)$ and $2^+D1^+(\rho K)$, for $1.0 \leq M_{K\pi\pi} \leq 1.6$ GeV, $0.05 \leq |t'| \leq$ ≤ 0.7 GeV^2. The curves are the results of a fit assuming a single resonance and no background: the fitted phases have been corrected for the variation of the reference phase, $1^+S0^+(K^*\pi)$.

Fig. 18 : Intensities and phases of 0^- waves for $1.0 \leq M_{K\pi\pi} \leq 1.8$ GeV, $0 \leq |t'| \leq 0.7$ GeV^2. The phases are measured relative to $1^+S0^+(K^*\pi)$. The curves show the result of fitting with a single resonance and a simple background in all three channels. The fitted phases have been corrected for the variation of the reference phase.

Fig. 19 : Dalitz plot boundary for $M_{K\pi\pi} = 1.8$ GeV, showing the full width at half-height bands for the resonances $K^*(890)$, $K^*(1430)$, ρ and f.

Fig. 20 : Intensities and phases of 2^- waves for $1.5 < M_{K\pi\pi} < 2.1$ GeV, $0 < |t'| < 0.7$ GeV^2. The phase of $2^-S0^+(K^{**}\pi)$ versus $1^+S0^+(\rho K)$ is plotted: the phases of the other 2^- waves are measured relative to $2^-S0^+(K^{**}\pi)$. The solid curves were obtained when fitting with one resonance and background, the broken curves when fitting with two resonances and background. If the $1^+S0^+(\rho K)$ phase is slowly varying, then the $1^+S0^+(K^{**}\pi)$ phase increases through $\sim 100°$ between $K\pi\pi$ masses of 1.7 and 1.9 GeV, and through more than 200° over the full range.

Fig. 21 : The intensity in $1^+D0^+(K^*\pi)$ and $1^+P0^+(\varepsilon K)$ for $1.0 < M_{K\pi\pi} < 2.1$ GeV, $0 < |t'| < 0.7$ GeV^2. The lower peak in $1^+D0^+(K^*\pi)$ is well explained within the two-resonance model for the Q region, the upper peak is stable against changes in the wave set. The upper peak in $1^+P0^+(\varepsilon K)$ dominates the structure in the Q region, but is contributed mostly by the flip wave. The total 1^+ intensity is stable (fig. 11).

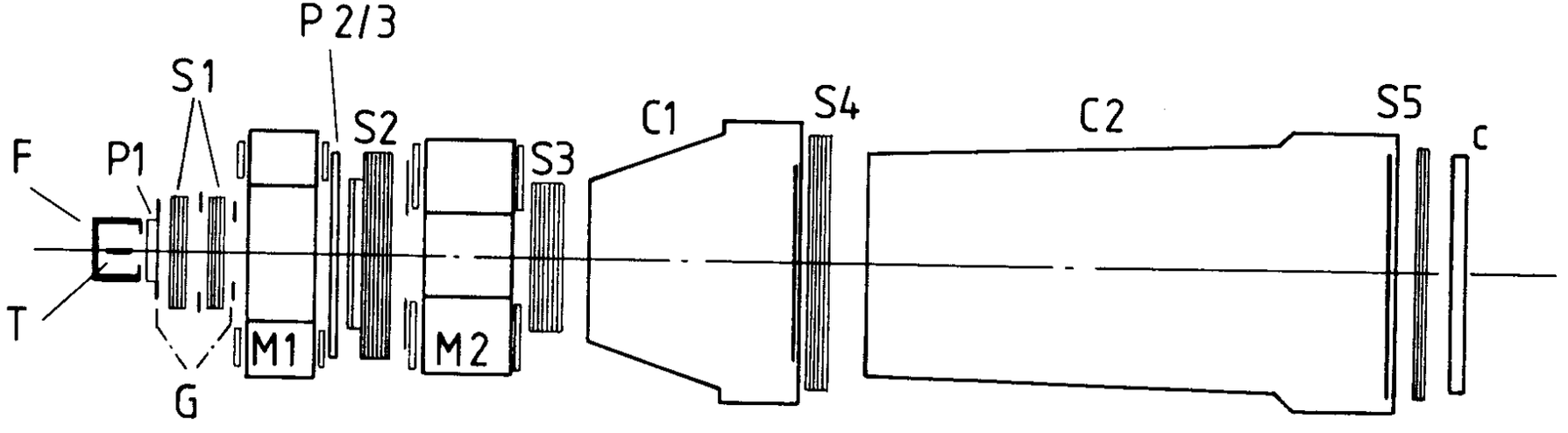

Fig. 1

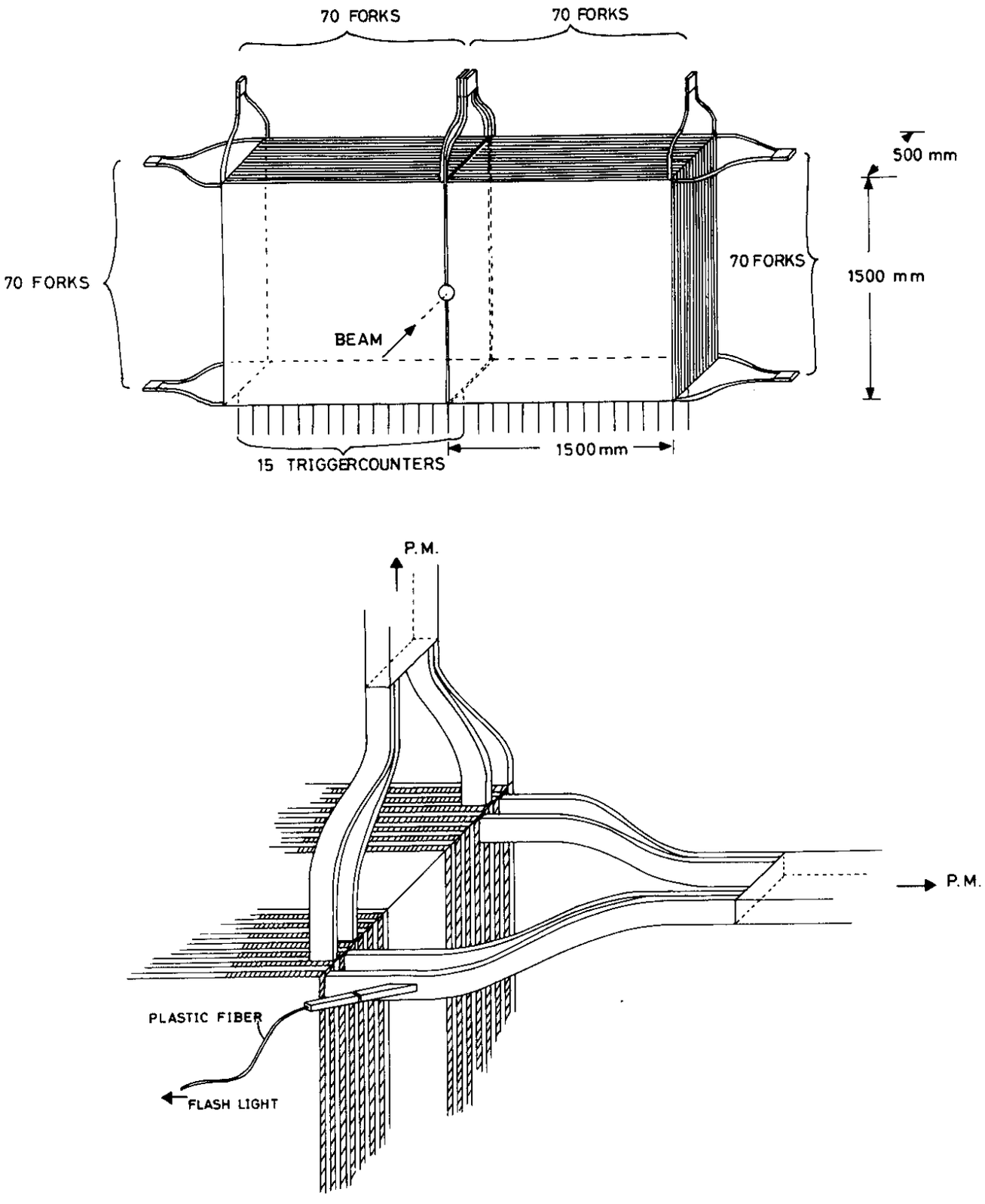
70 FORKS
70 FORKS
500 mm
70 FORKS
70 FORKS
1500 mm
BEAM
15 TRIGGERCOUNTERS
1500 mm
P.M.
P.M.
PLASTIC FIBER
FLASH LIGHT

Fig. 2

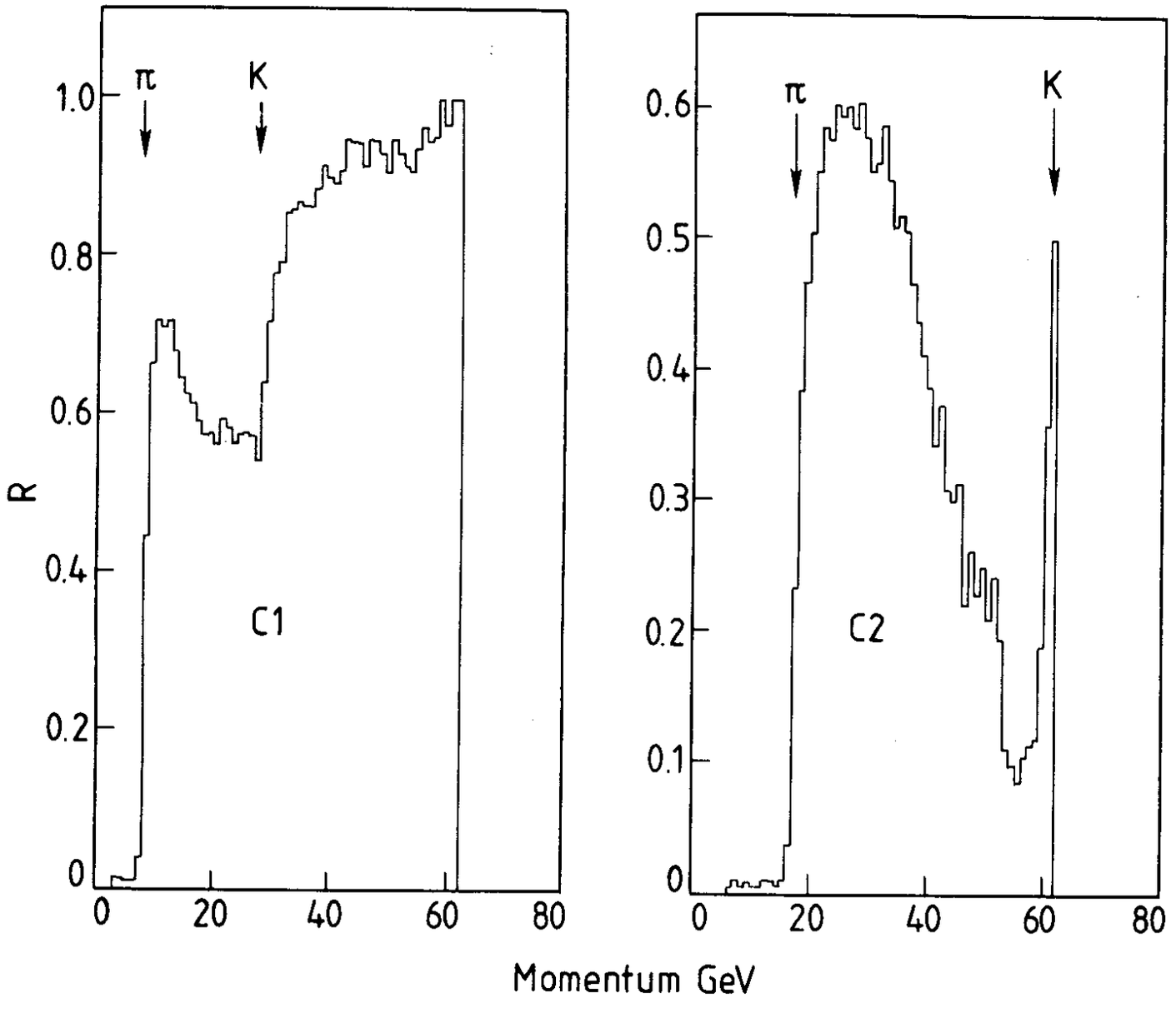
π
K
1.0
0.8
0.6
0.4
0.2
0
R
C1
0
20
40
60
80
π
K
0.6
0.5
0.4
0.3
0.2
0.1
0
C2
0
20
40
60
80
Momentum GeV

Fig. 3

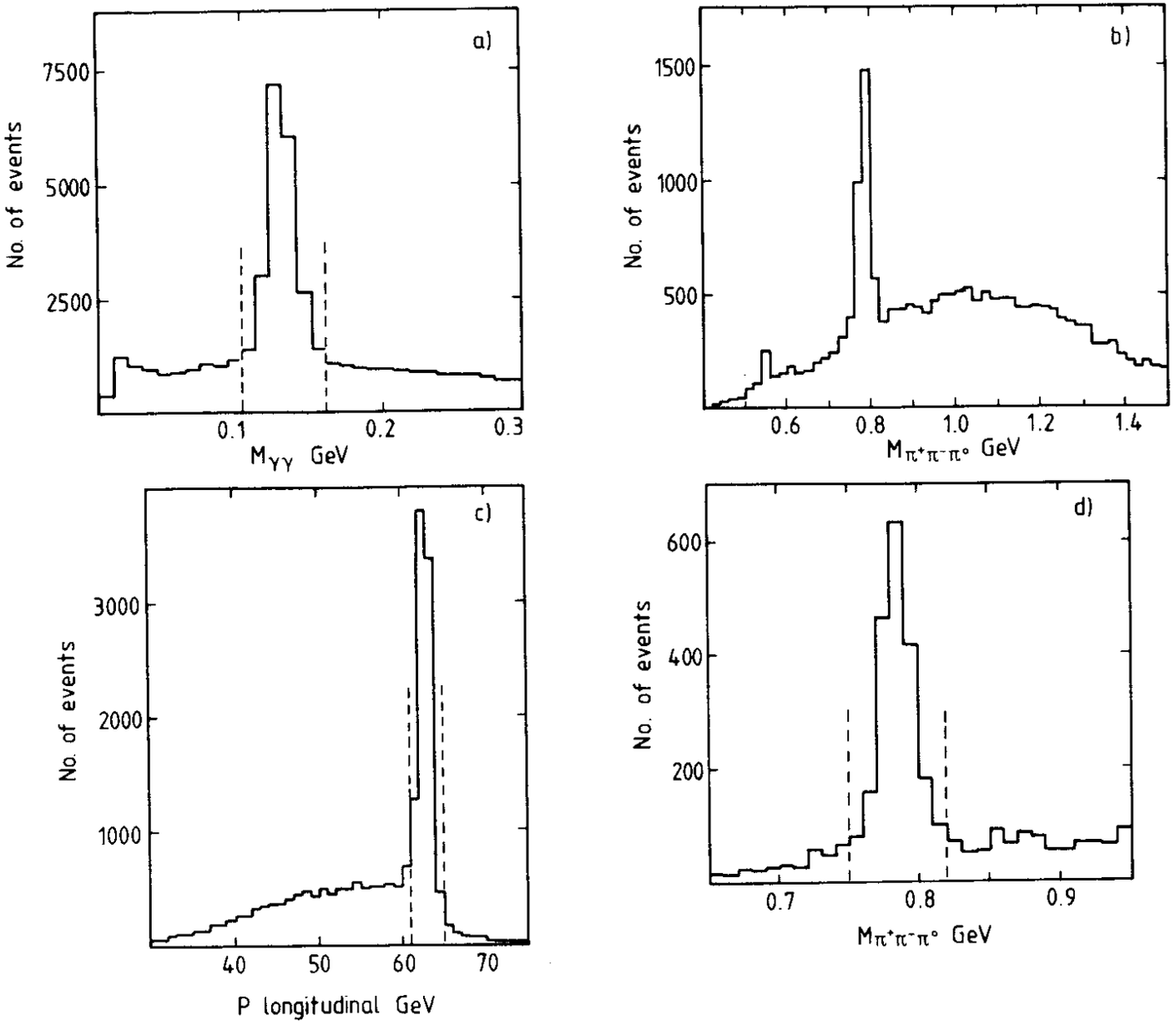
a)
No. of events
7500
5000
2500
0.1
0.2
0.3
$M_{\gamma\gamma}$ GeV
b)
No. of events
1500
1000
500
0.6
0.8
1.0
1.2
1.4
$M_{\pi^+\pi^-\pi^\circ}$ GeV
c)
No. of events
3000
2000
1000
40
50
60
70
P longitudinal GeV
d)
No. of events
600
400
200
0.7
0.8
0.9
$M_{\pi^+\pi^-\pi^\circ}$ GeV

Fig. 4

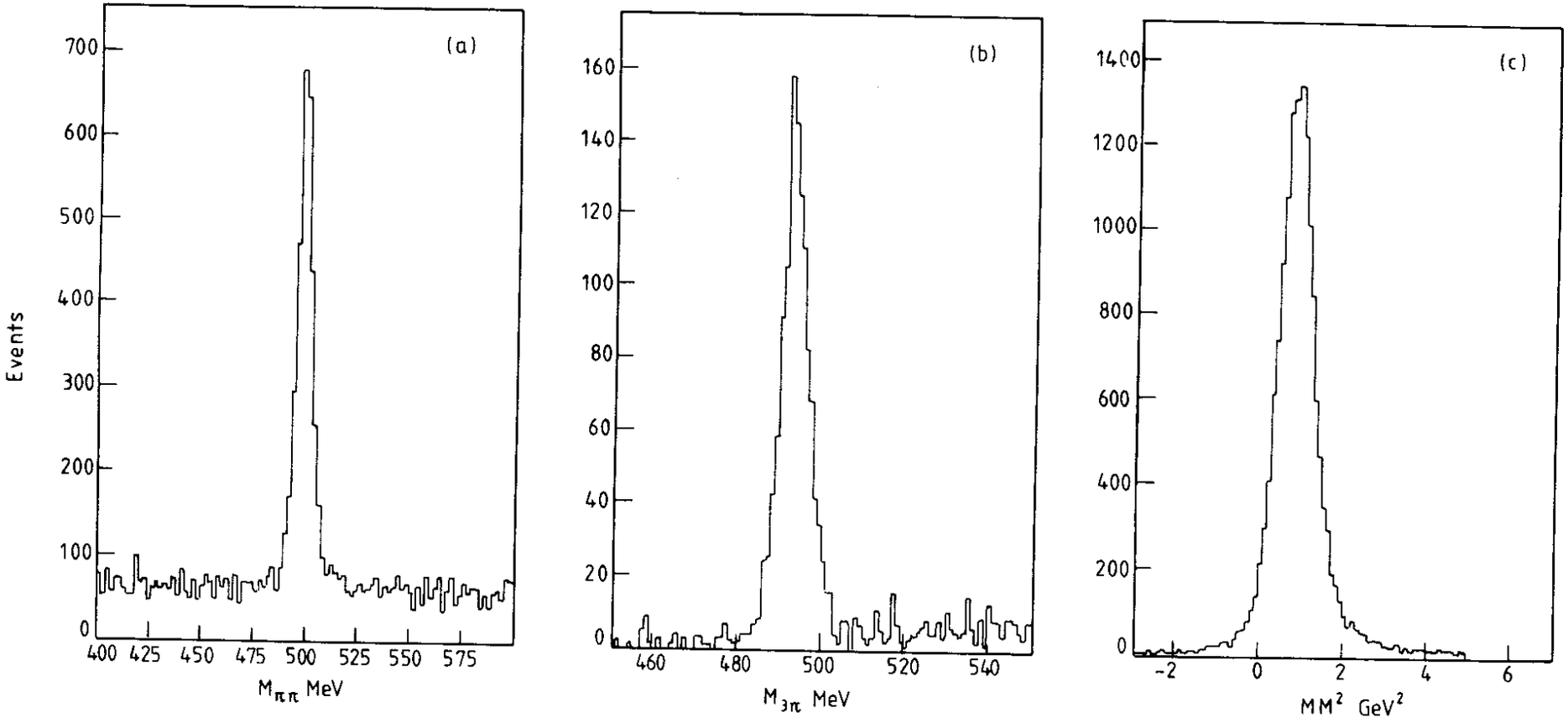
(a)
Events
700
600
500
400
300
200
100
0
400 425 450 475 500 525 550 575
$M_{\pi\pi}$ MeV
(b)
160
140
120
100
80
60
40
20
0
460 480 500 520 540
$M_{3\pi}$ MeV
(c)
1400
1200
1000
800
600
400
200
0
-2 0 2 4 6
MM^2 GeV^2

Fig. 5

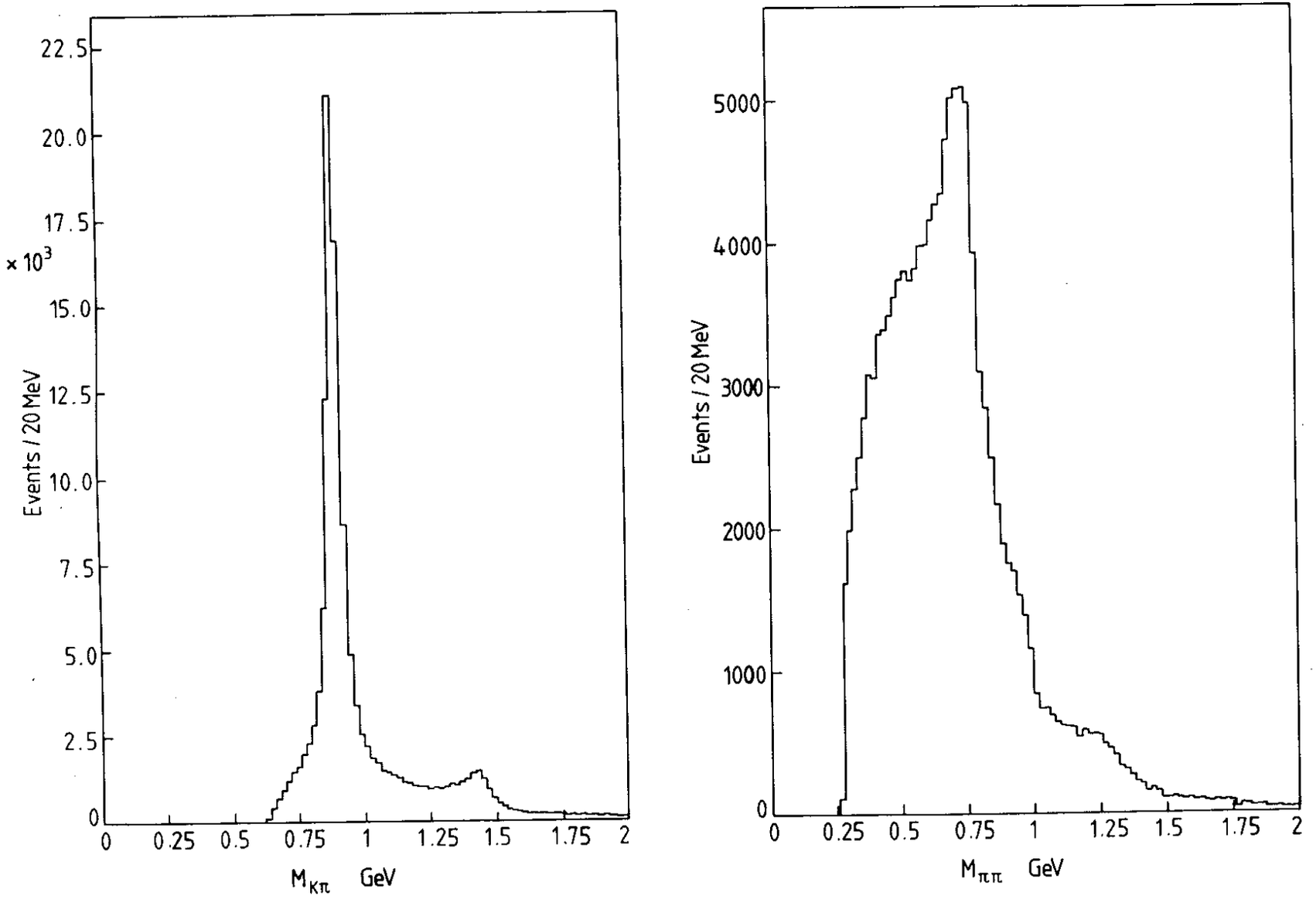
22.5
20.0
17.5
× 10³
15.0
12.5
10.0
7.5
5.0
2.5
0
Events / 20 MeV
0 0.25 0.5 0.75 1 1.25 1.5 1.75 2
M_Kπ GeV
5000
4000
3000
2000
1000
0
Events / 20 MeV
0 0.25 0.5 0.75 1 1.25 1.5 1.75 2
M_ππ GeV

Fig. 6

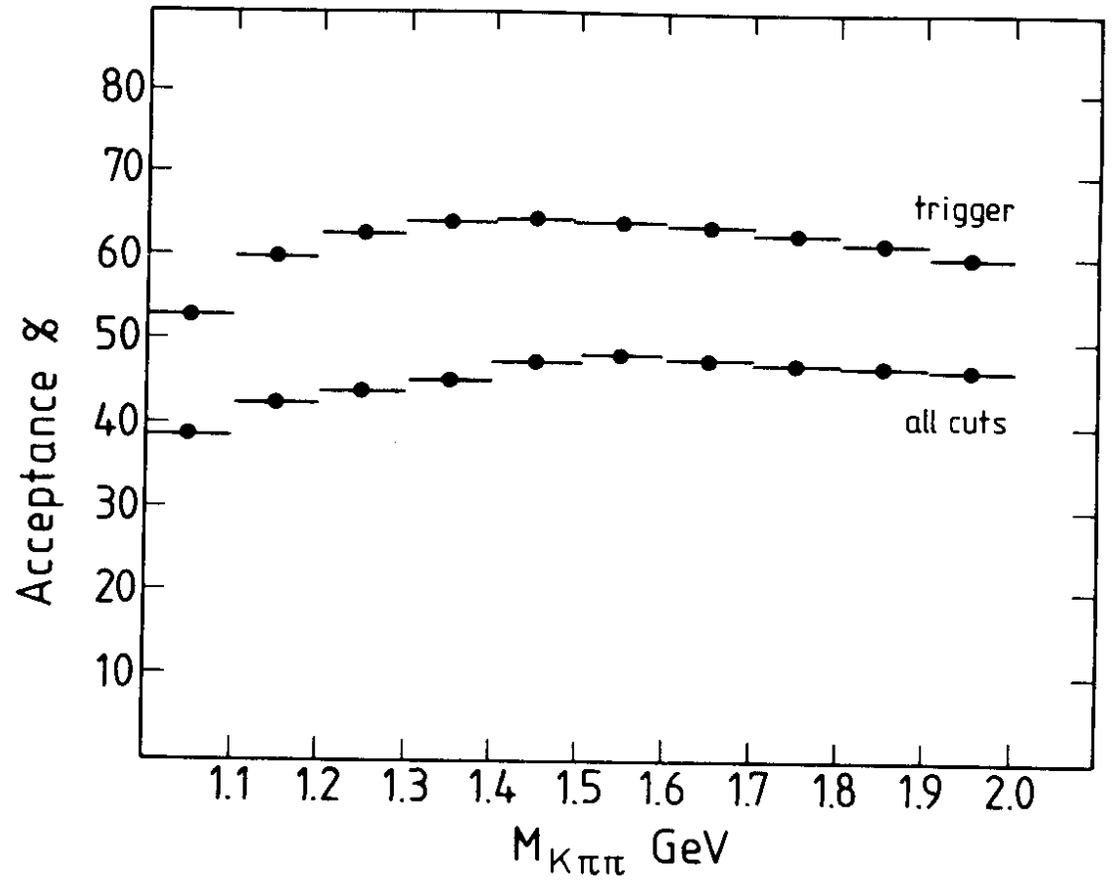
Acceptance %
80
70
60
50
40
30
20
10
trigger
all cuts
1.1
1.2
1.3
1.4
1.5
1.6
1.7
1.8
1.9
2.0
$M_{K\pi\pi}$ GeV

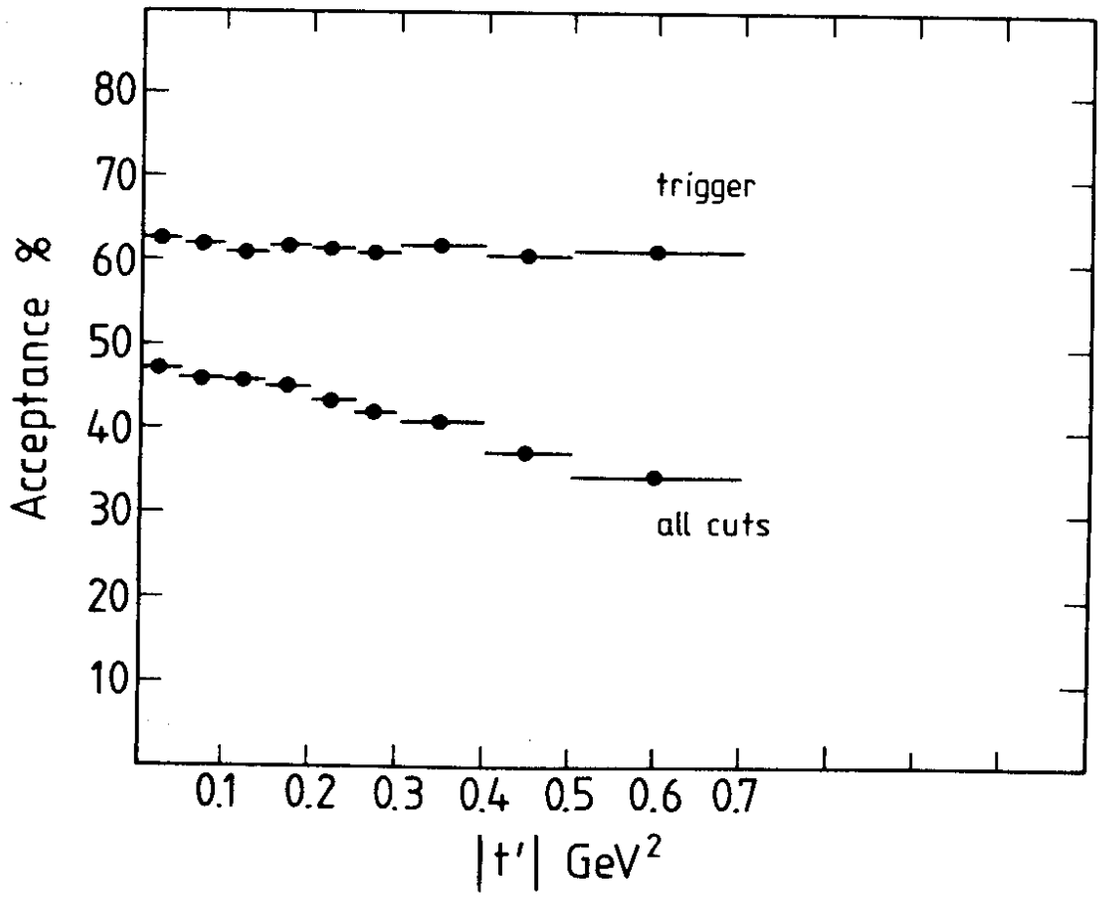
Acceptance %
80
70
60
50
40
30
20
10
trigger
all cuts
0.1
0.2
0.3
0.4
0.5
0.6
0.7
$|t'|$ GeV^2

Fig. 7

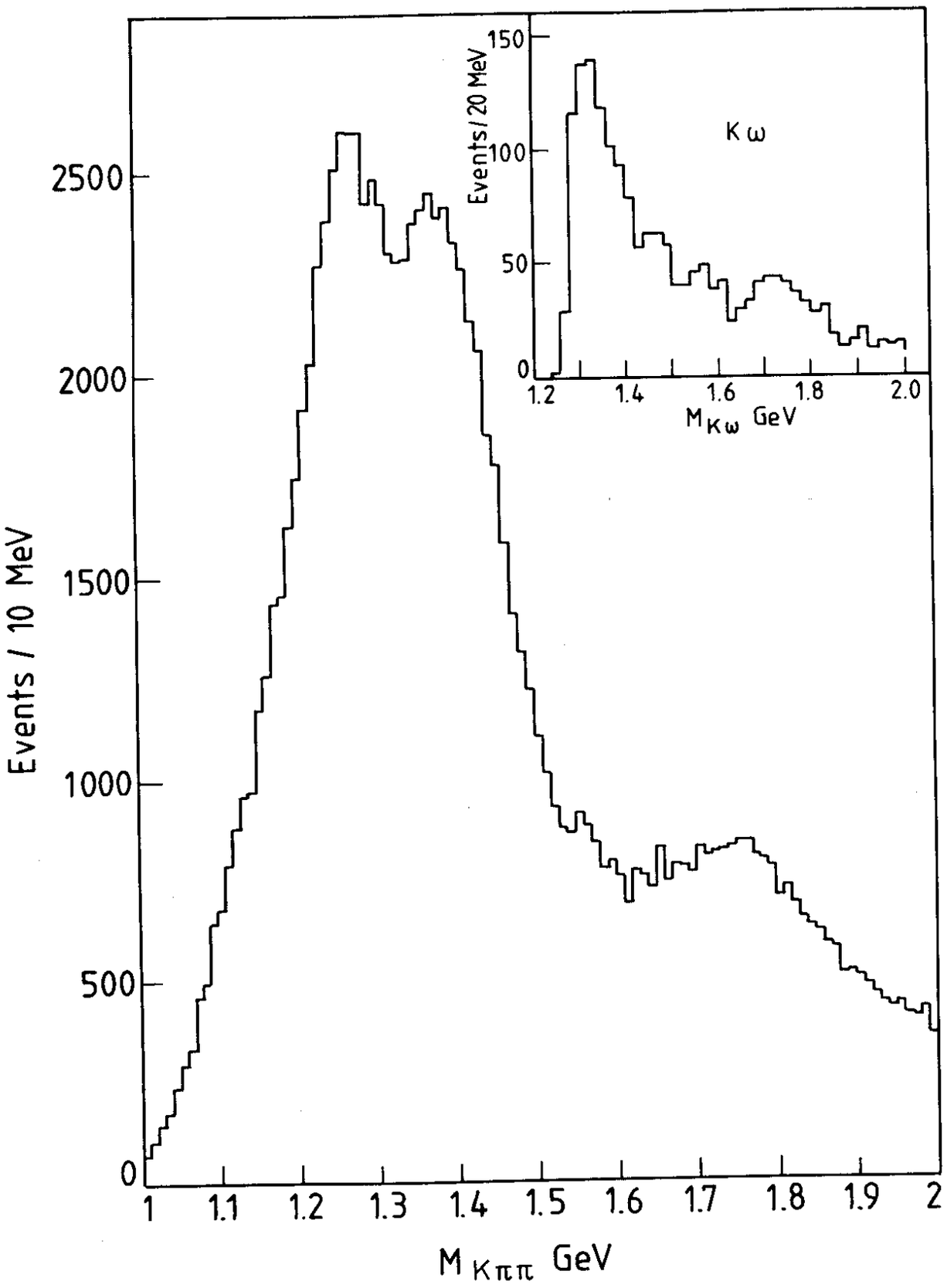
Events / 10 MeV
2500
2000
1500
1000
500
0
1
1.1
1.2
1.3
1.4
1.5
1.6
1.7
1.8
1.9
2
M Kππ GeV
Events/20 MeV
150
100
50
0
1.2
1.4
1.6
1.8
2.0
M Kω GeV
Kω

Fig. 8

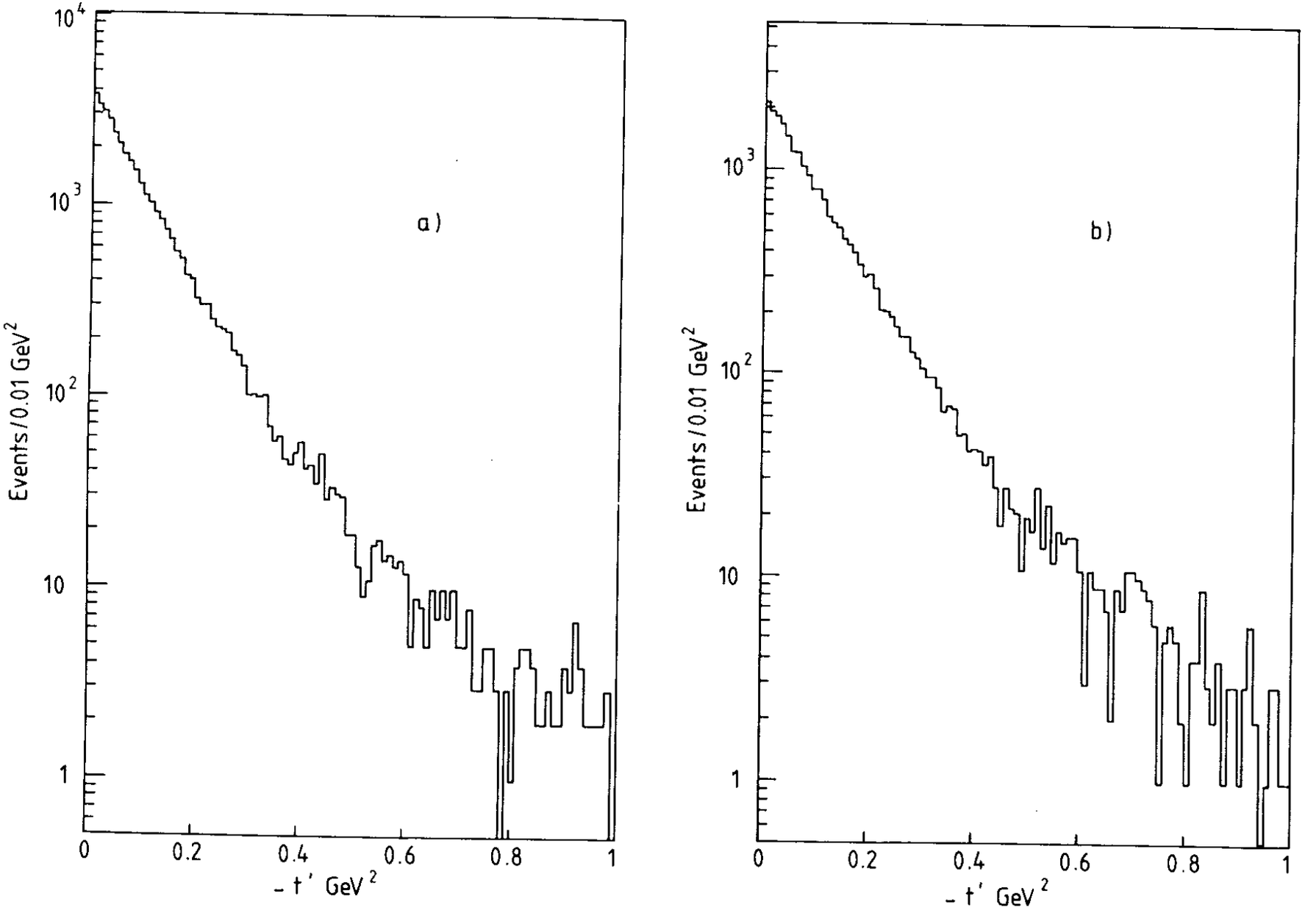

Fig. 9

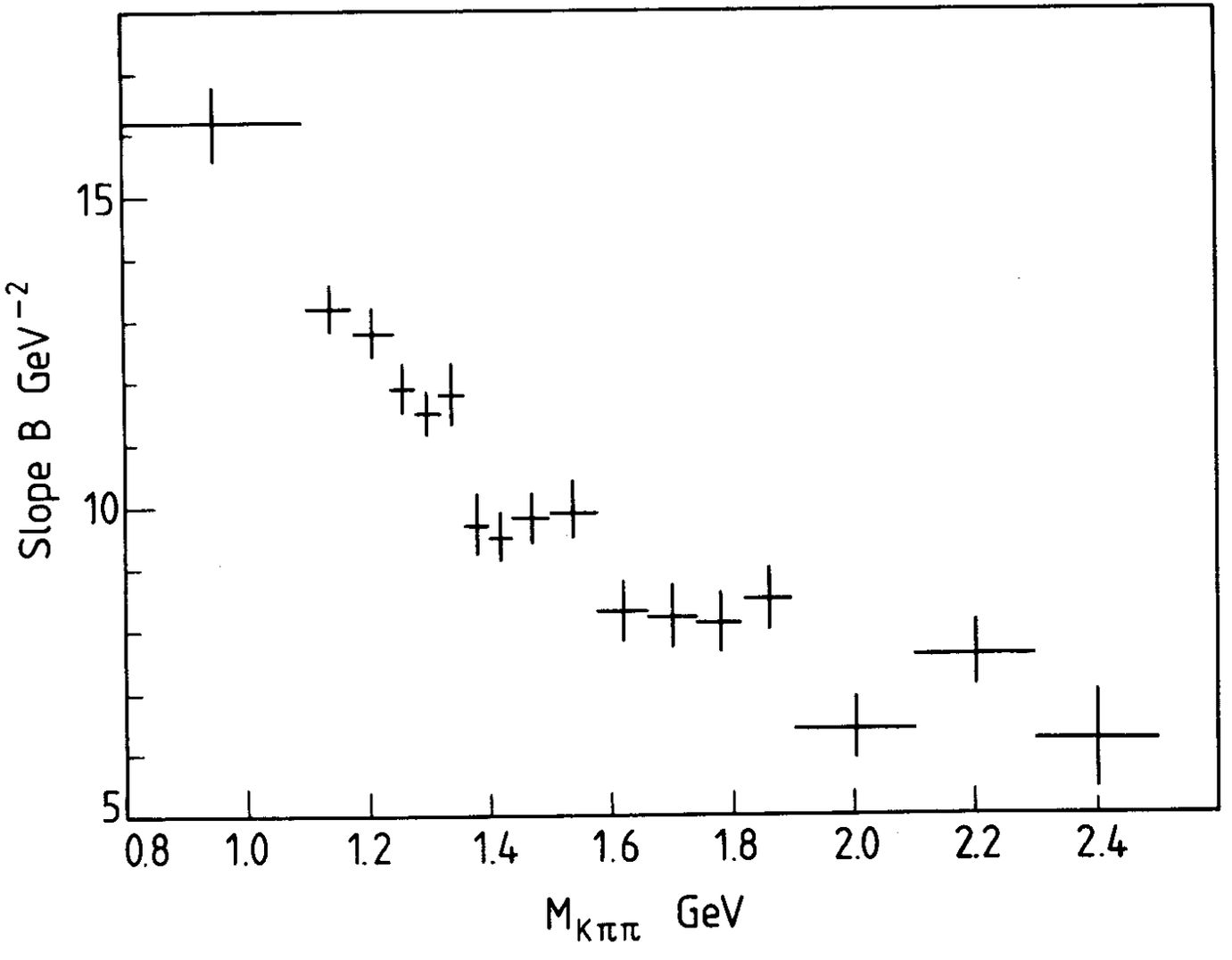

Fig. 10

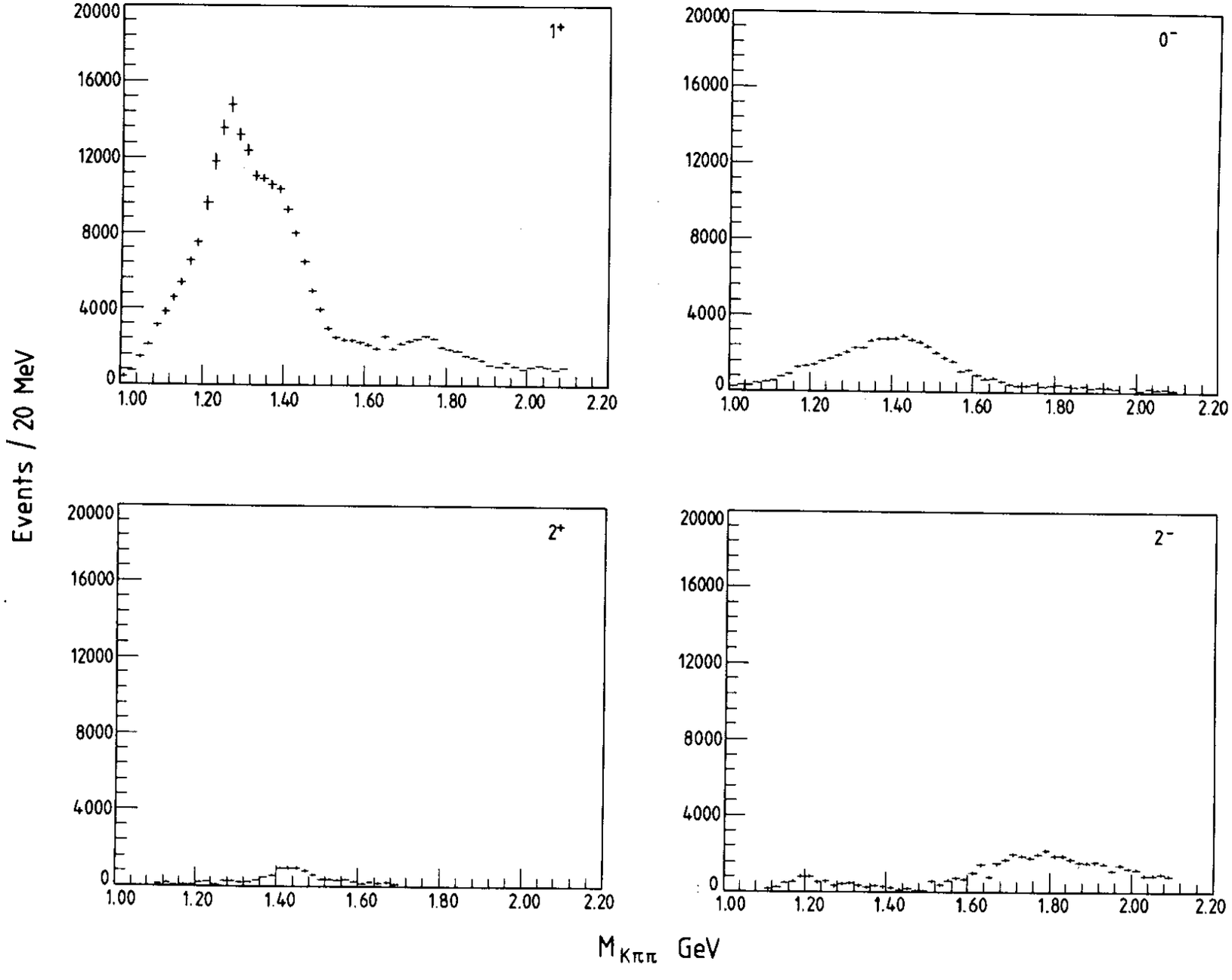

Fig. 11

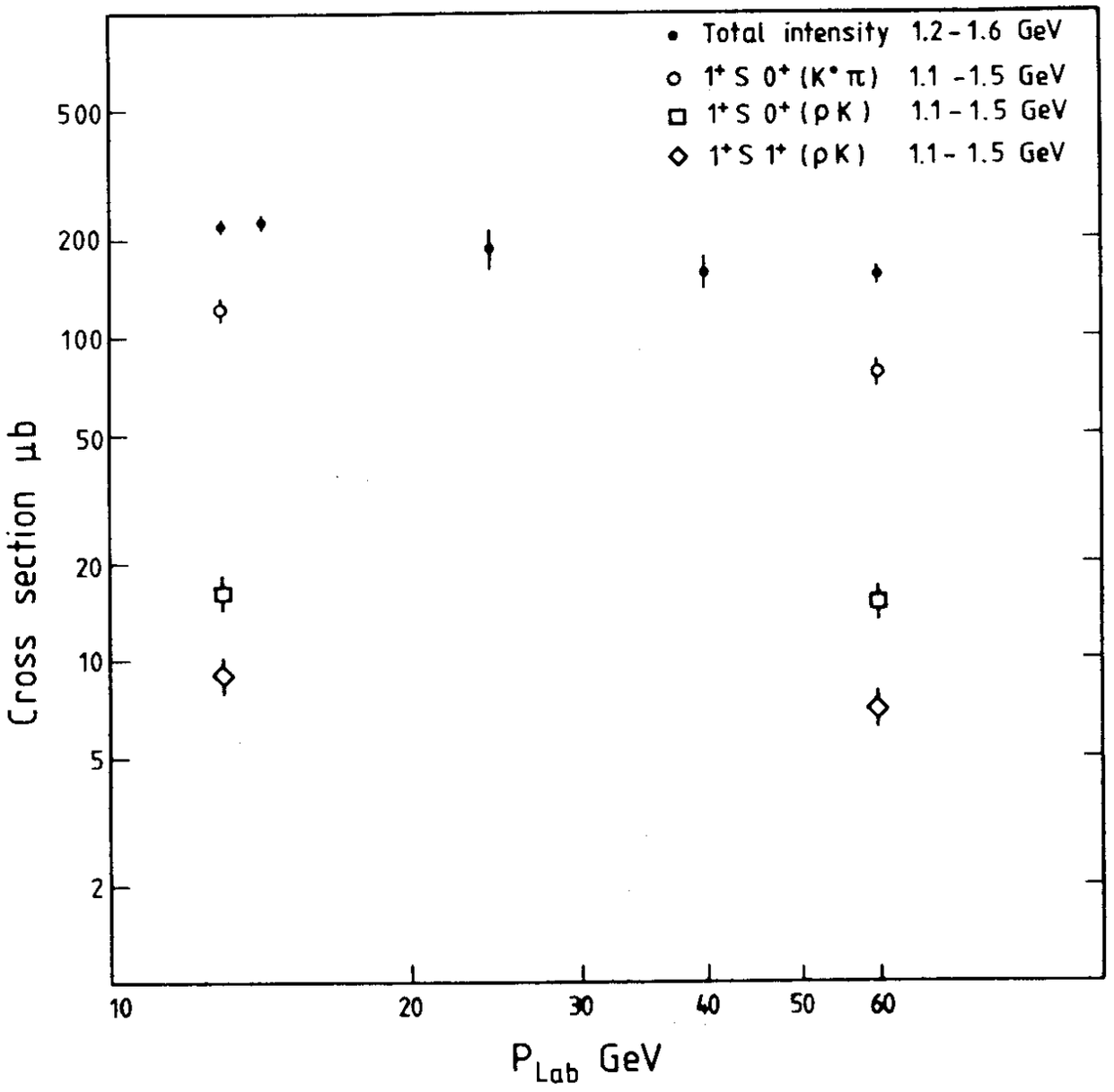
• Total intensity 1.2 - 1.6 GeV
o 1⁺ S 0⁺ (K*π) 1.1 - 1.5 GeV
□ 1⁺ S 0⁺ (ρK) 1.1 - 1.5 GeV
◇ 1⁺ S 1⁺ (ρK) 1.1 - 1.5 GeV
Cross section μb
500
200
100
50
20
10
5
2
10
20
30
40
50
60
P Lab GeV

Fig. 12

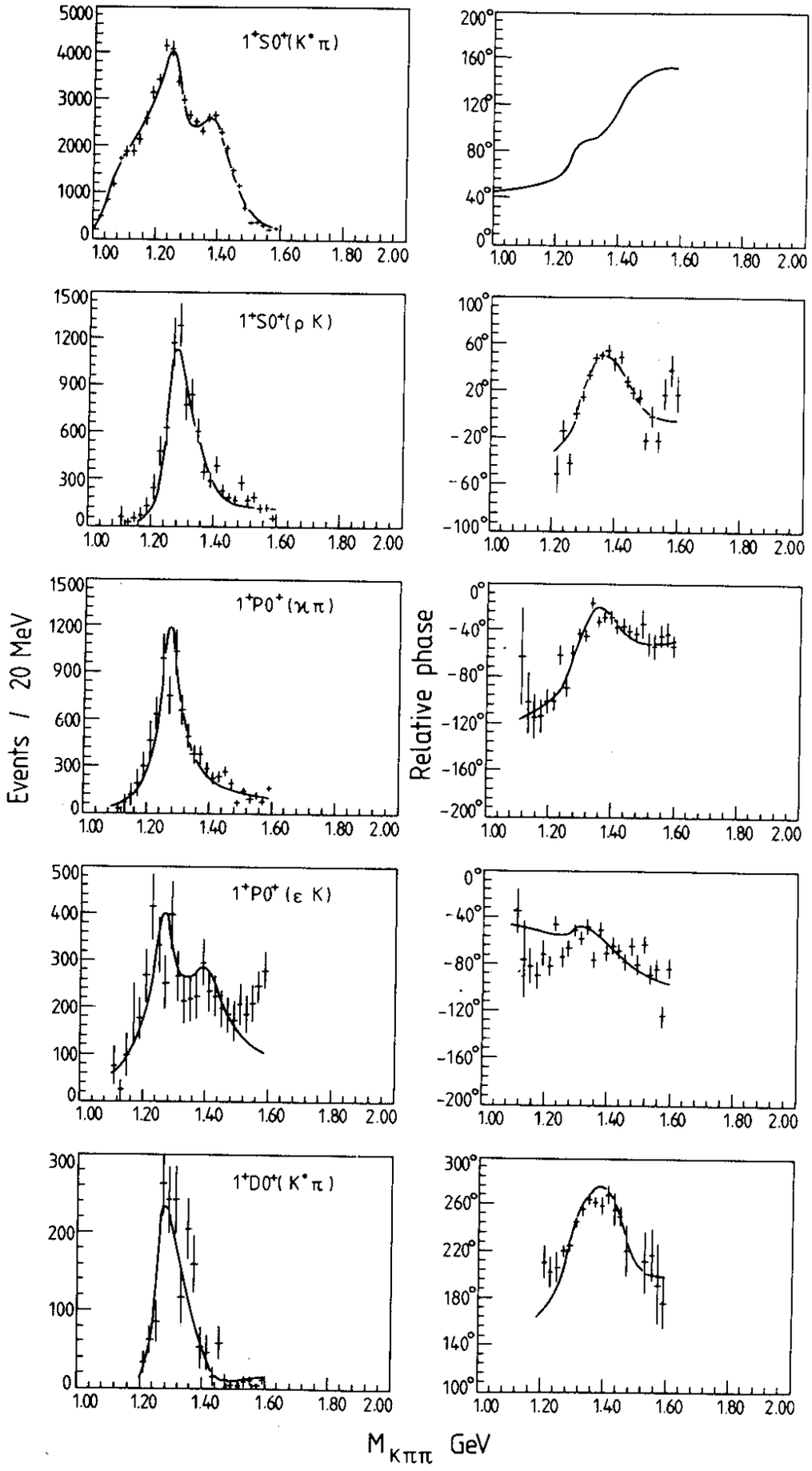
1⁺S0⁺(K*π)
1⁺S0⁺(ρ K)
1⁺P0⁺(κπ)
1⁺P0⁺(ε K)
1⁺D0⁺(K*π)
Events / 20 MeV
Relative phase
M Kππ GeV

Fig. 13

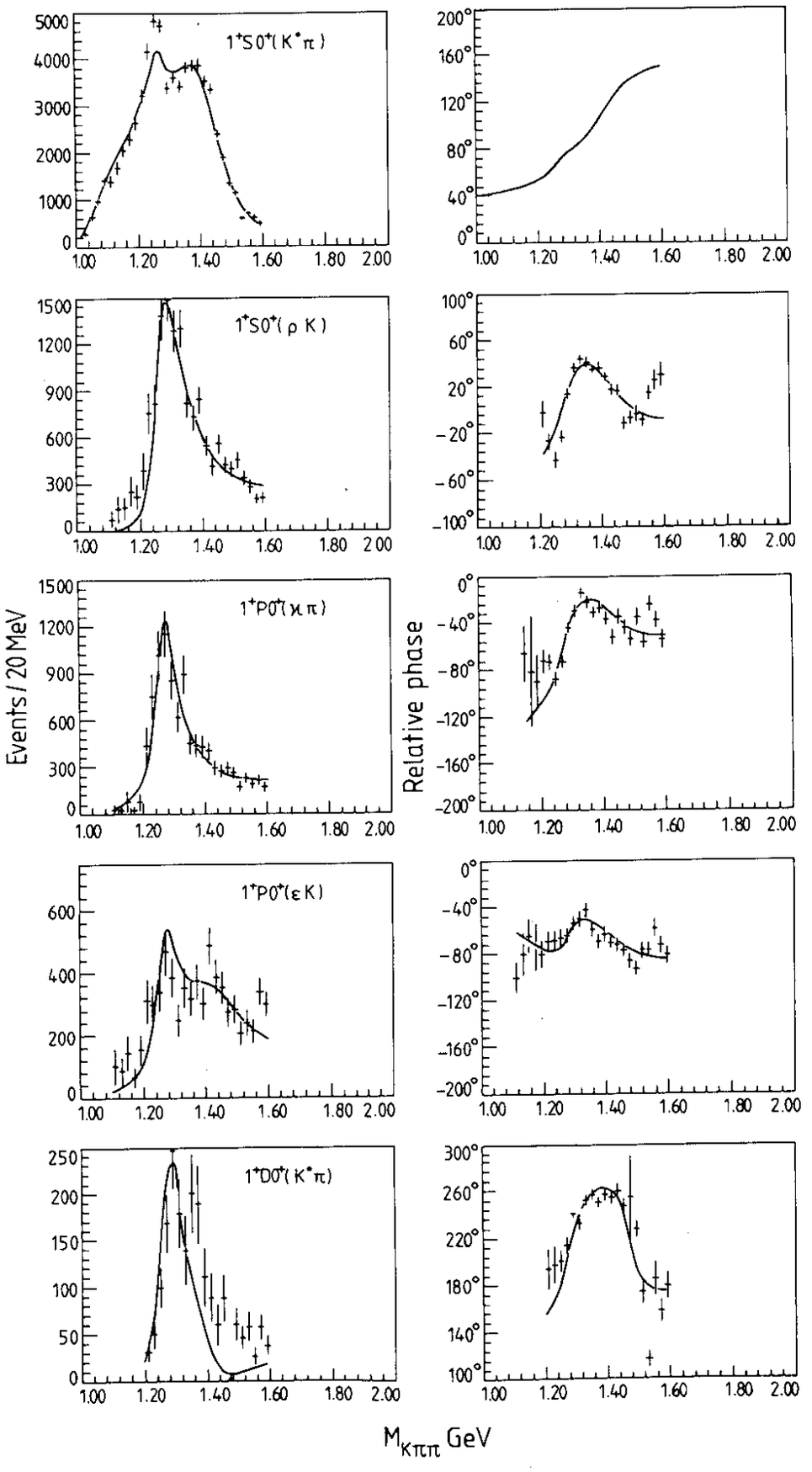
1⁺S0⁺(K*π)
1⁺S0⁺(ρK)
1⁺P0⁺(κπ)
1⁺P0⁺(εK)
1⁺D0⁺(K*π)
Events / 20 MeV
Relative phase
M_Kππ GeV

Fig. 14

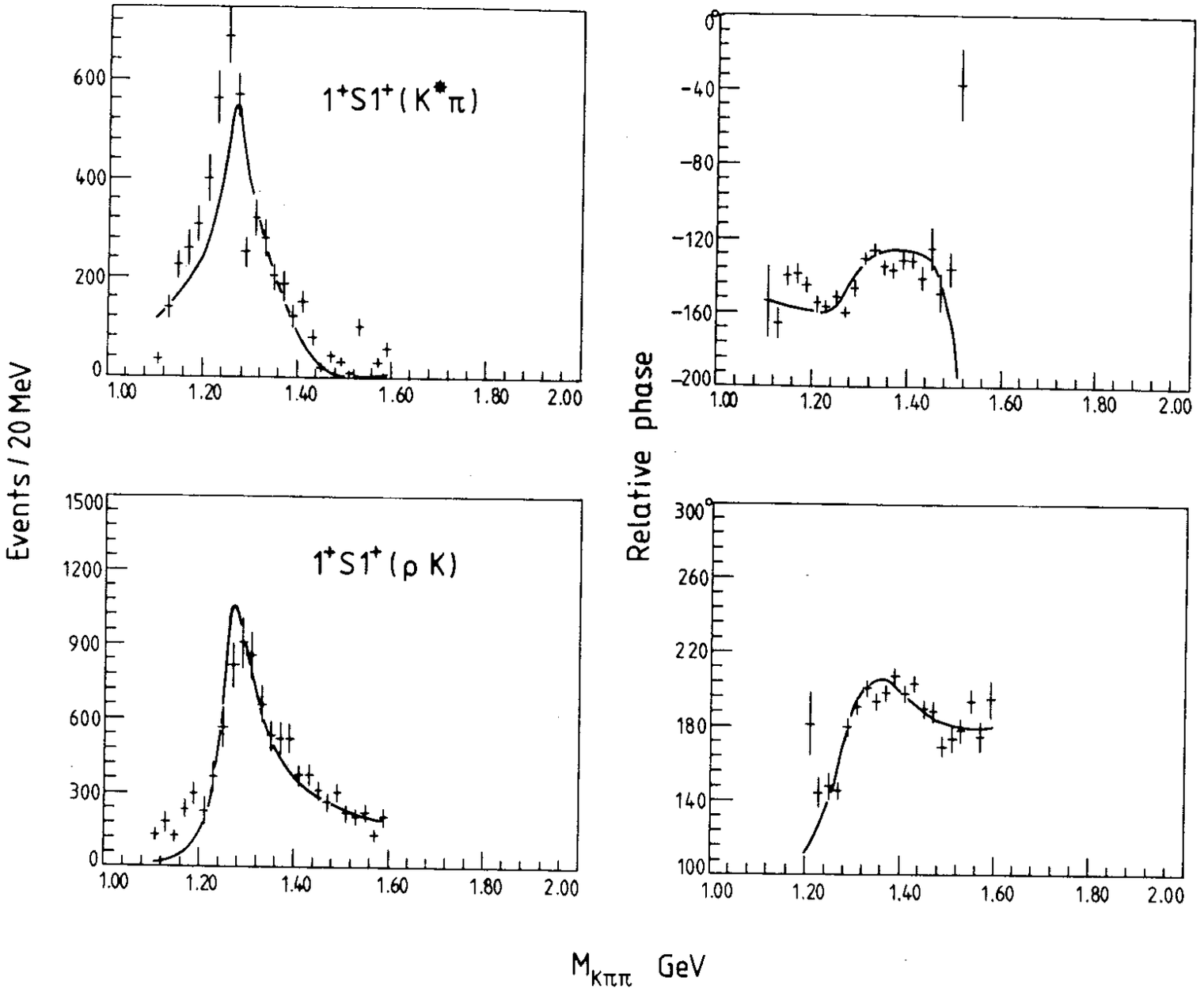

Fig. 15

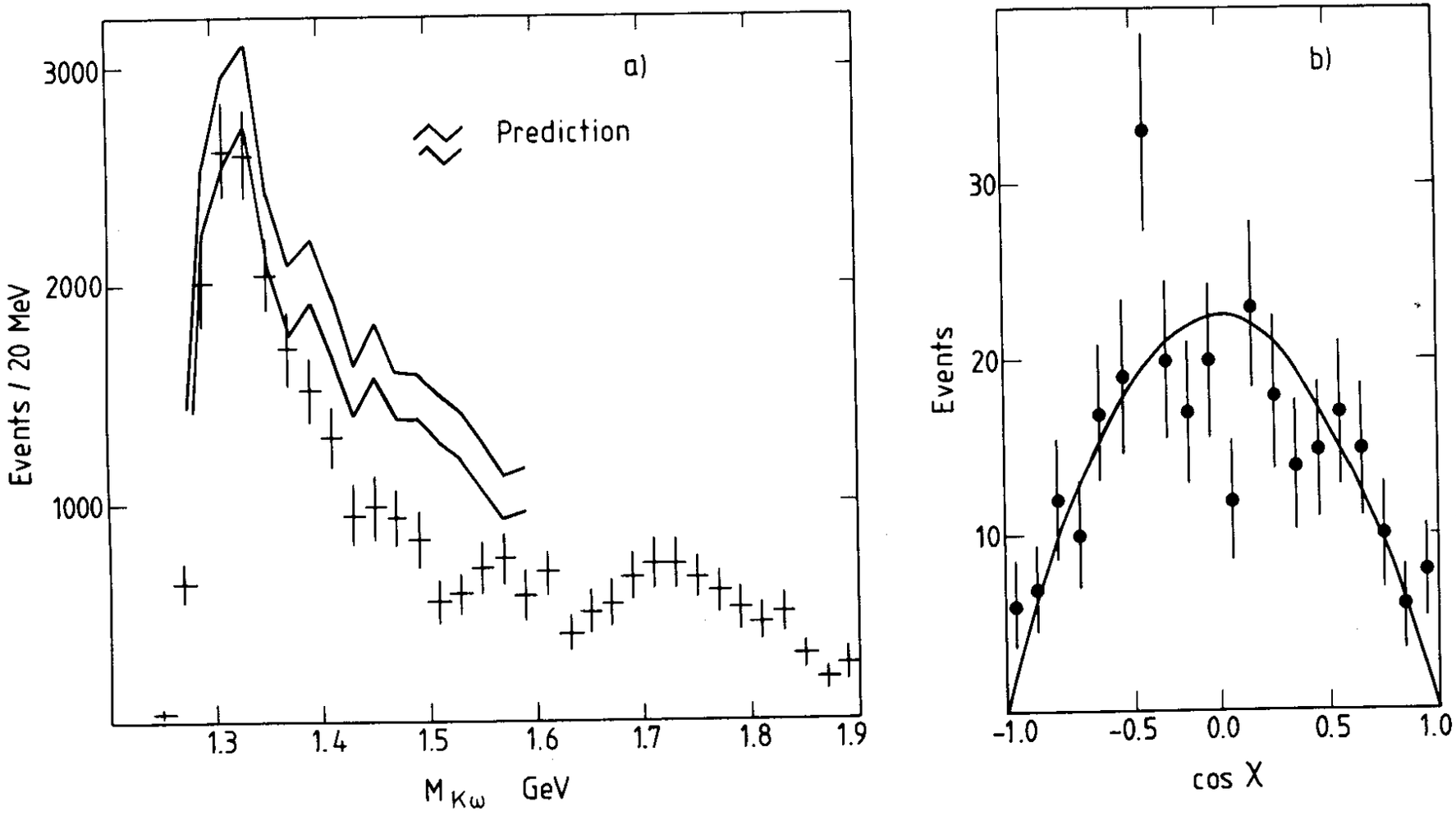
a)
Prediction
Events / 20 MeV
3000
2000
1000
1.3
1.4
1.5
1.6
1.7
1.8
1.9
$M_{K\omega}$ GeV
b)
Events
30
20
10
-1.0
-0.5
0.0
0.5
1.0
cos X

Fig. 16

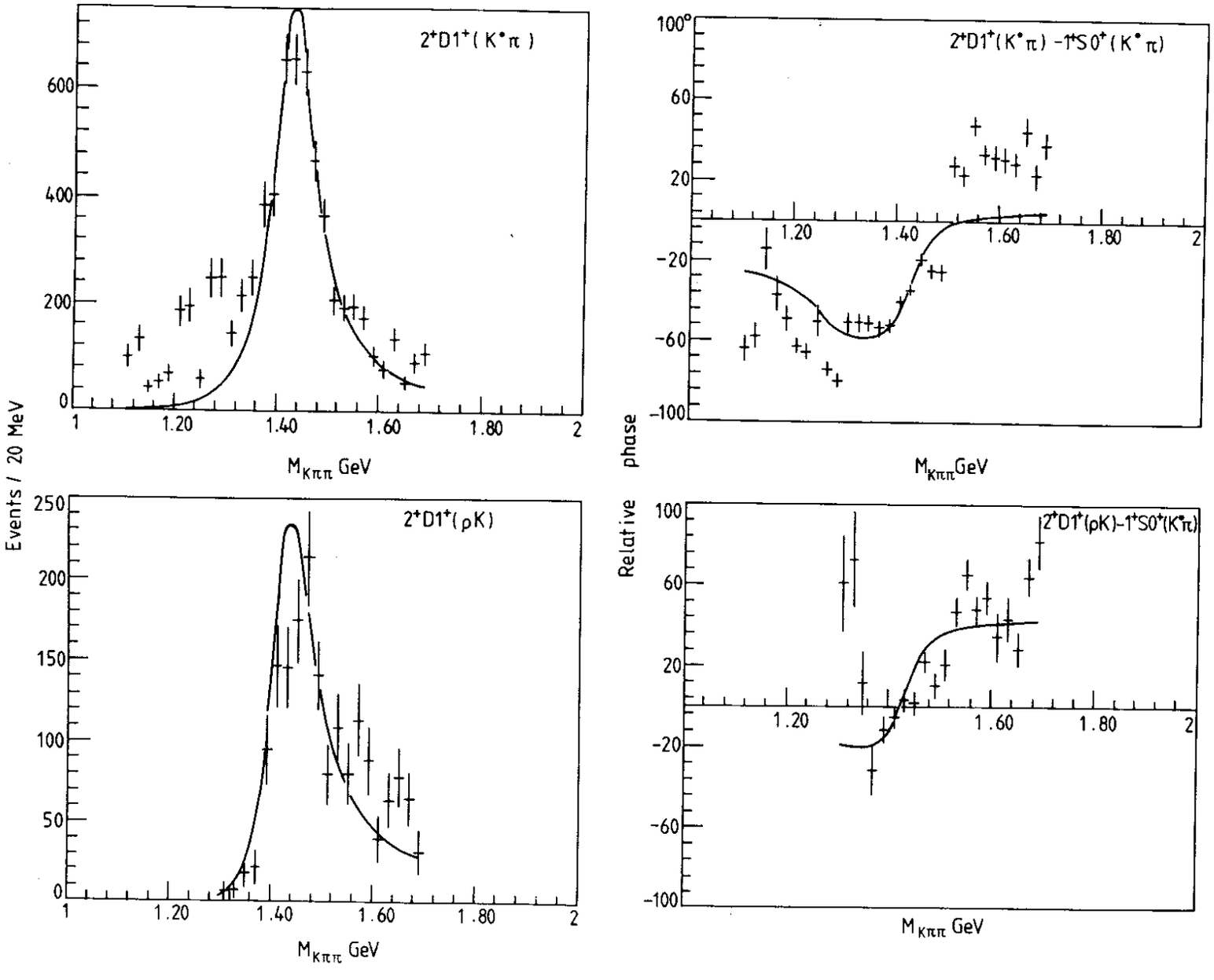
2⁺D1⁺(K*π)
Events / 20 MeV
M_Kππ GeV
2⁺D1⁺(K*π) -1⁺S0⁺(K*π)
phase
M_Kππ GeV
2⁺D1⁺(ρK)
M_Kππ GeV
2⁺D1⁺(ρK)-1⁺S0⁺(K*π)
Relative
M_Kππ GeV

Fig. 17

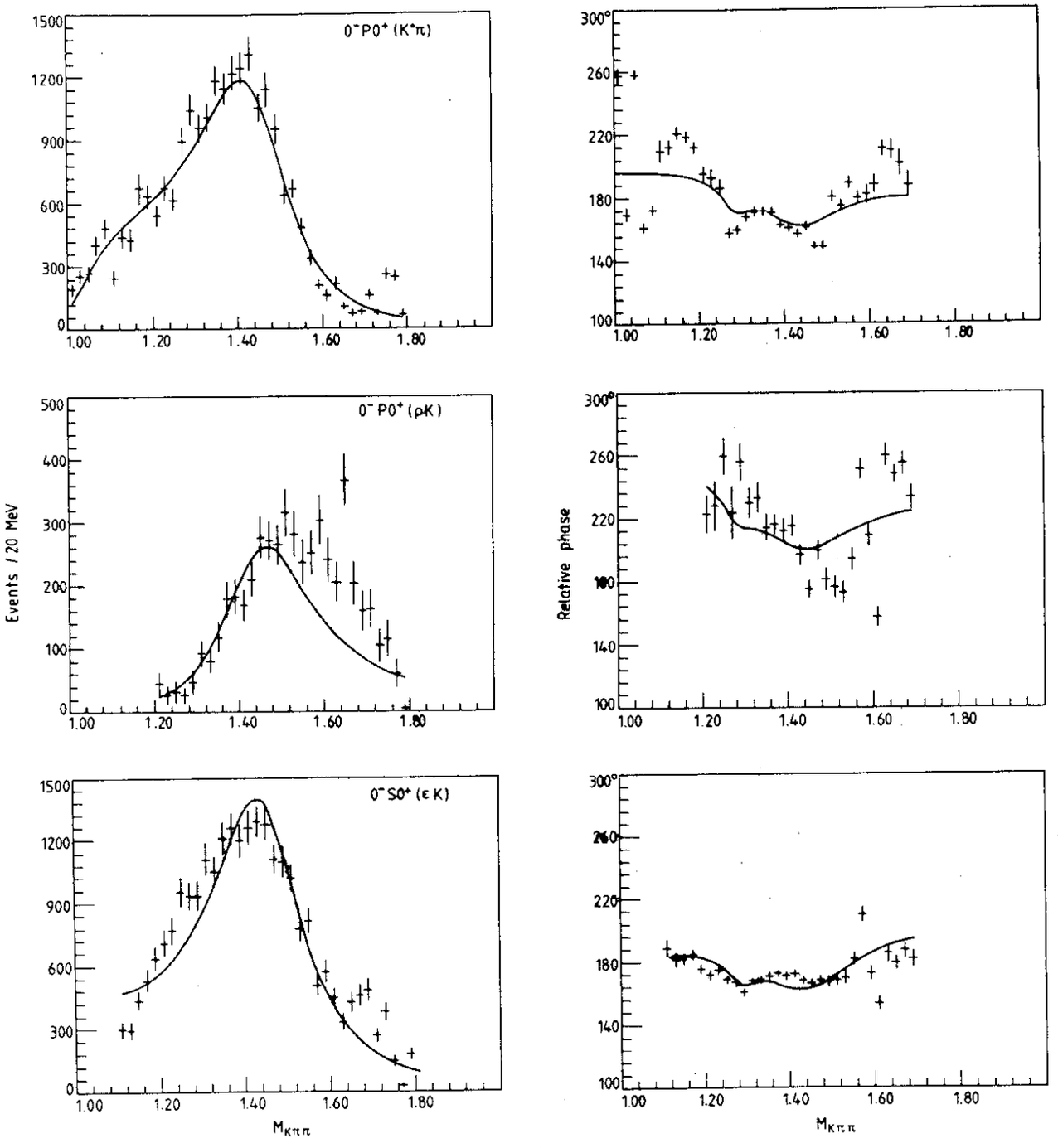

Fig. 18

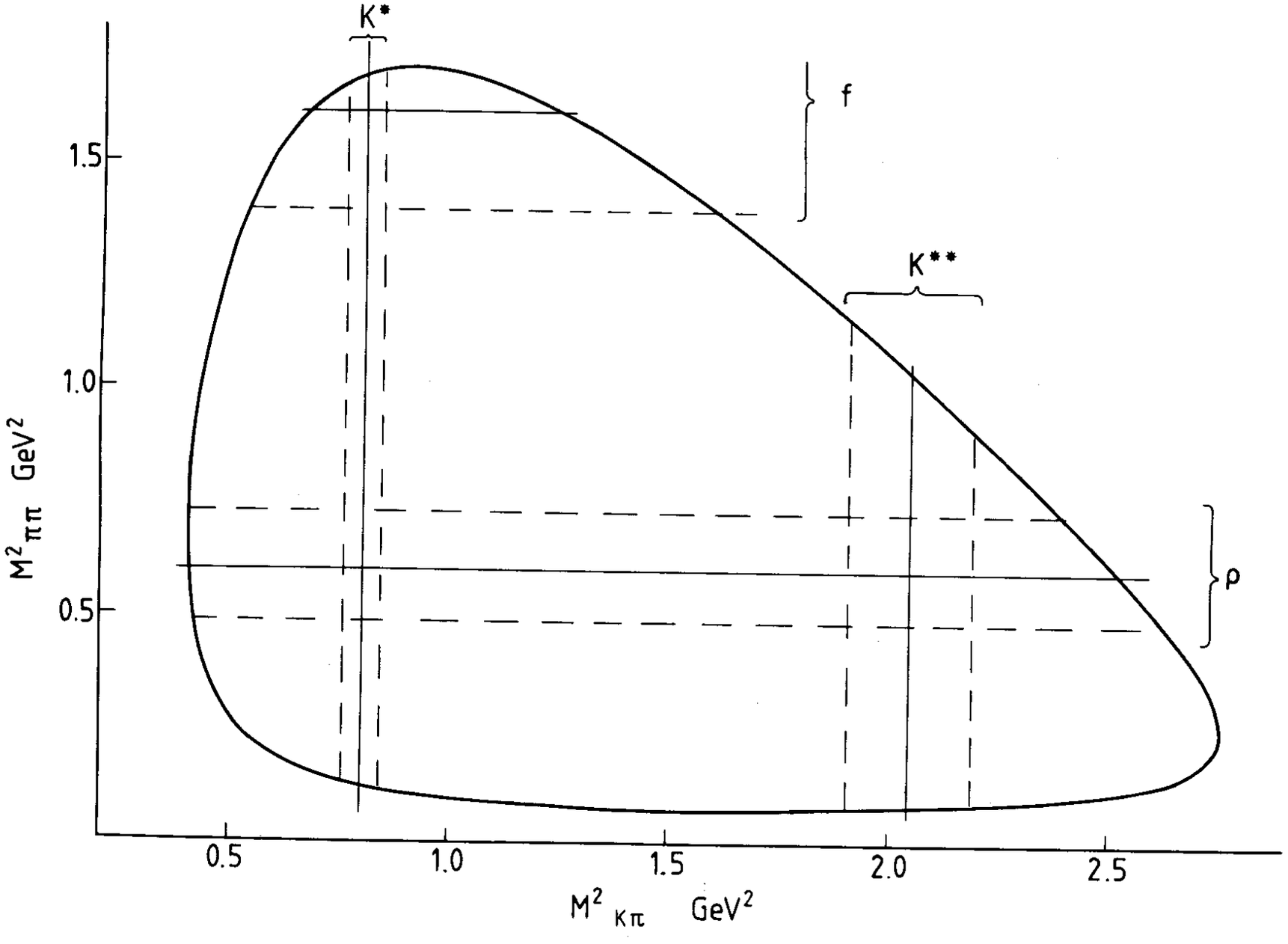

Fig. 19

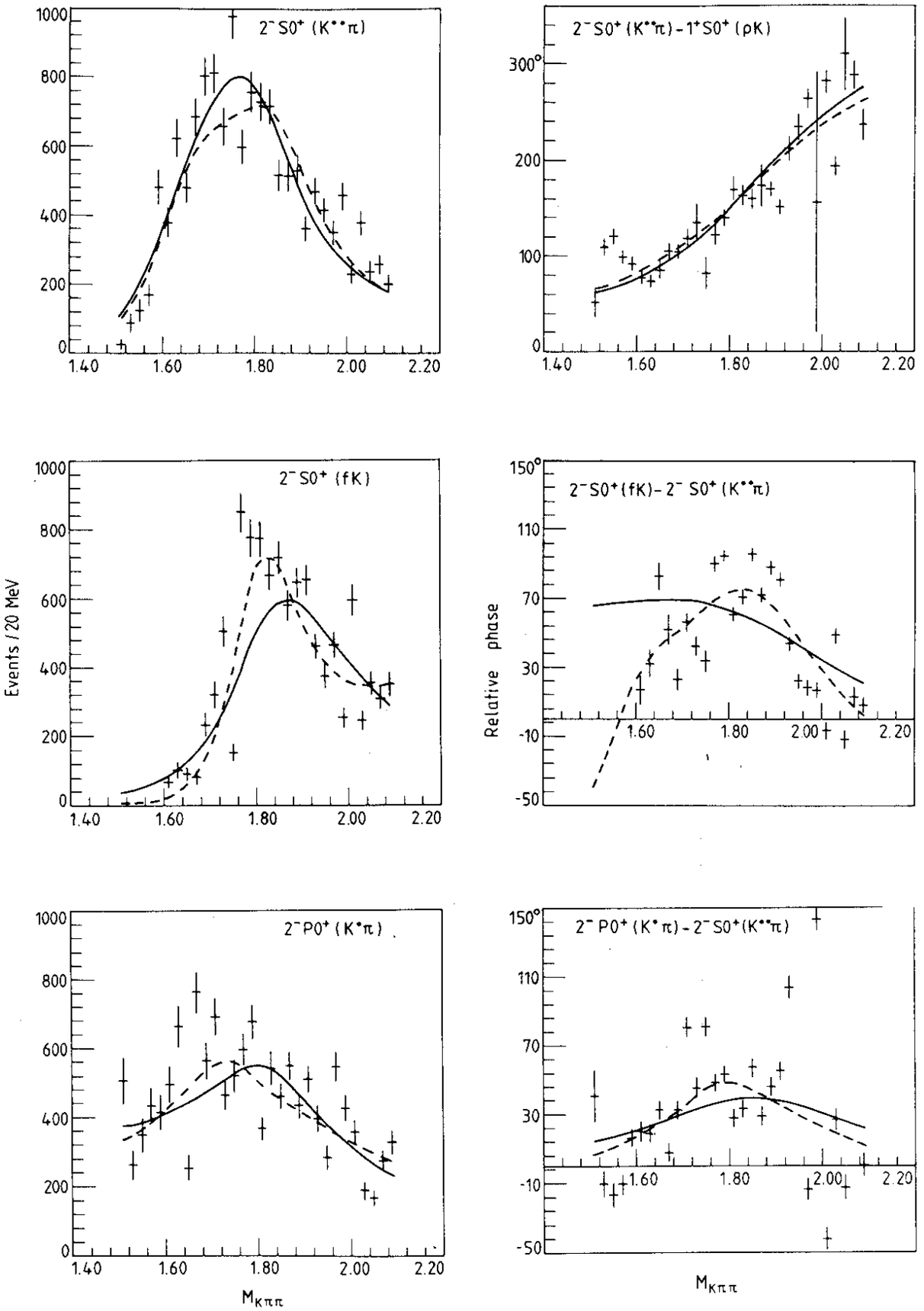
2⁻S0⁺ (K**π)
2⁻S0⁺ (K**π) - 1⁺S0⁺ (ρK)
2⁻S0⁺ (fK)
2⁻S0⁺(fK) - 2⁻ S0⁺ (K**π)
2⁻P0⁺ (K*π)
2⁻ P0⁺ (K*π) - 2⁻S0⁺(K**π)
Events / 20 MeV
Relative phase
M Kππ
M Kππ

Fig. 20

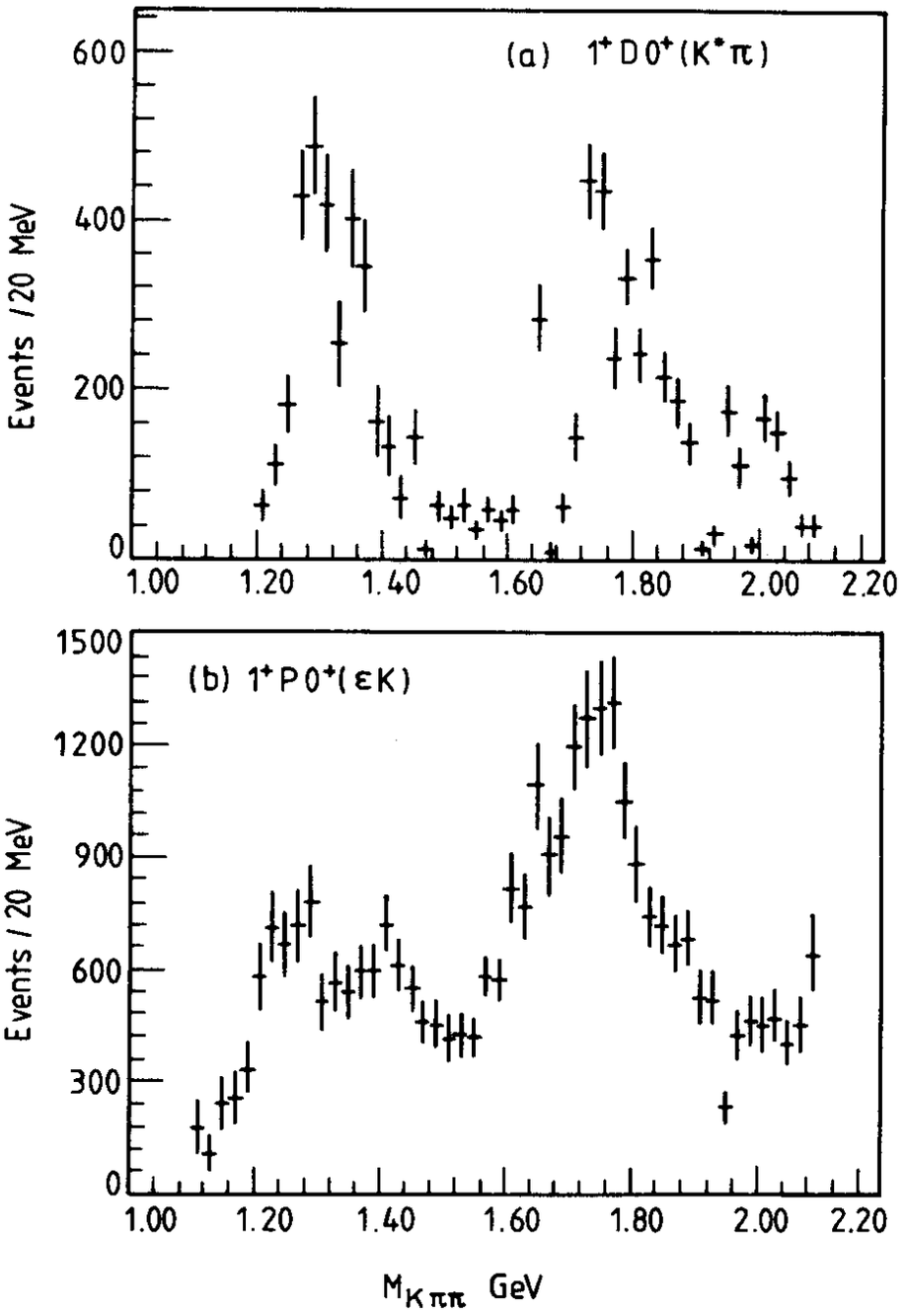
(a) 1⁺ D 0⁺ (K*π)
Events /20 MeV
600
400
200
0
1.00
1.20
1.40
1.60
1.80
2.00
2.20
(b) 1⁺ P 0⁺ (εK)
Events / 20 MeV
1500
1200
900
600
300
0
$M_{K\pi\pi}$ GeV

Fig. 21